Chapter 6
X-Ray Emission from Pulsars and Neutron Stars

Werner Becker

6.1 Introduction

The idea of *neutron stars* can be traced back to the early 1930s, when Subrahmanyan Chandrasekhar discovered that there is no way for a collapsed stellar core with a mass more than 1.4 times the solar mass, $M_\odot$, to hold itself up against gravity once its nuclear fuel is exhausted. This implies that a star left with $M > 1.4\ M_\odot$ (the *Chandrasekhar limit*) would keep collapsing and eventually disappear from view.

After the discovery of the neutron by James Chadwick in 1932 scientists speculated on the possible existence of a *star composed entirely of neutrons*, which would have a radius of the order of $R \sim (\hbar/m_n c)(\hbar c/G m_n^2)^{1/2} \sim 3 \times 10^5$ cm. In view of the peculiar stellar parameters, Lev Landau called these objects "unheimliche Sterne" (weird stars), expecting that they would never be observed because of their small size and expected low optical luminosity.

Walter Baade and Fritz Zwicky were the first who proposed the idea that neutron stars could be formed in *supernovae*. First models for the structure of neutron stars were worked out in 1939 by Oppenheimer and Volkoff (Oppenheimer–Volkoff limit). Unfortunately, their pioneering work did not predict anything astronomers could actually observe, and the idea of neutron stars was not taken serious by the astronomical community. Neutron stars therefore had remained in the realm of imagination for nearly a quarter of a century, until in the 1960s a series of epochal discoveries were made in high-energy and radio astronomy [20, 73, 148].

X-rays and gamma-rays can only be observed from above the earth's atmosphere,[1] which requires detectors to operate from high flying balloons, rockets or satellites. One of the first X-ray detectors brought to space was launched by Herbert Friedman and his team at the Naval Research Laboratory in order to investigate the

W. Becker
Max-Planck Institut für extraterr. Physik, Giessenbachstrasse 1, 85741 Garching, Germany
e-mail: web@mpe.mpg.de

---

[1] X-rays are absorbed at altitudes 20–100 km.

W. Becker (ed.), *Neutron Stars and Pulsars,* Astrophysics and Space Science Library 357,

influence of solar activity on the propagation of radio signals in the earth's atmosphere. Using simple proportional counters put on old V-2 (captured in Germany after the World War II) and Aerobee rockets, they were the first who detected X-rays from the very hot gas in the solar corona. However, the intensity of this radiation was found to be a factor 10^6 lower than that measured at optical wavelengths. In the late 1950s, it was therefore widely believed that all other stars, much more distant than the Sun, should be so faint in X-rays that further observations at that energy range would be hopeless.

On the other hand, results from high-energy cosmic ray experiments suggested that there exist celestial objects (e.g., supernova remnants) which produce high-energy cosmic rays in processes which, in turn, may also produce X-rays and gamma-rays [112, 113]. These predictions were confirmed in 1962, when the team led by Bruno Rossi and Riccardo Giacconi accidentally detected X-rays from Sco X-1.

With the aim to search for fluorescent X-ray photons from the Moon,[2] they launched an Aerobee rocket on 12 June 1962 from White Sands (New Mexico) with three Geiger counters as payload, each having a $\sim 100^\circ$ field of view and an effective collecting area of about $10\,\mathrm{cm}^2$ [51]. The experiment detected X-rays not from the Moon but from a source located in the constellation Scorpio, dubbed as Sco X-1, which is now known as the brightest extra-solar X-ray source in the sky. Evidence for a weaker source in the Cygnus region and the first evidence for the existence of a diffuse isotropic X-ray background was also reported from that experiment [52]. Subsequent flights launched to confirm these first results detected Tau X-1, a source in the constellation Taurus which coincided with the Crab supernova remnant [25].

Among the various processes proposed for the generation of the detected X-rays was *thermal radiation from the surface of a hot neutron star* [35], and searching for this radiation has become a strong motivation for further development of X-ray astronomy. However, the X-ray emission from the Crab supernova remnant was found to be of a finite angular size (~ 1 arcmin) whereas a neutron star was expected to appear as a point source.

Thus, the early X-ray observations were not sensitive enough to prove the existence of neutron stars. This was done a few years later by radio astronomers.

In 1967, Jocelyn Bell, a graduate student under the supervision of Anthony Hewish at the Cambridge University of England, came across a series of pulsating radio signals while using a radio telescope specially constructed to look for rapid variations in the radio emission of quasars. These radio pulses, 1.32 s apart, with remarkable clock-like regularity, were emitted from an unknown source in the sky at right ascension $19^{\mathrm{h}}\,20^{\mathrm{m}}$ and declination $+23^\circ$. Further observations refined the pulsating period to 1.33730113 s. The extreme precision of the period suggested at first that these signals might be generated by extraterrestrial intelligence. They

---

[2] The Moon was selected as a target because it was expected that a state-of-the-art detector available at that time would not be sensitive enough to detect X-rays from extra-solar sources. "We felt [...] that it would be very desirable to consider some intermediate target which could yield concrete results while providing a focus for the development of more advanced instrumentation which ultimately would allow us to detect cosmic X-ray sources" [51].

were subsequently dubbed as LGM1, an acronym for "Little Green Man 1" [20]. However, as a few more similar sources had been detected, it became clear that a new kind of celestial objects was discovered. The link between these pulsating radio sources, which were called *pulsars*, and fast spinning neutron stars was provided by Franco Pacini [120, 121] and Thomas Gold [54, 55]. Pacini, then a young postdoc at the Cornell University, had published a paper a few months before the discovery by Bell and Hewish in which he proposed that the *rapid rotation of a highly magnetized neutron star* could be the source of energy in the Crab Nebula. This prediction was based on the pioneering work of Hoyle, Narlikar and Wheeler [74], who had proposed that a magnetic field of 10^{10} G might exist on a neutron star at the center of the Crab Nebula. The most fundamental ideas on the nature of the pulsating radio sources were published by Gold [54, 55] in two seminal *Nature* papers. In these papers Gold introduced the concept of the *rotation-powered pulsar* which radiates at the expense of its rotational energy (pulsar spins down as rotational energy is radiated away) and recognized that the rotational energy is lost via electromagnetic radiation of the rotating magnetic dipole and emission of relativistic particles. The particles are accelerated in the pulsar magnetosphere along the curved magnetic field lines and emit the observed intense curvature and synchrotron radiation.[3]

The discovery of the first radio pulsar was very soon followed by the discovery of the two most famous pulsars, the fast 33-ms pulsar in the Crab Nebula [145] and the 89-ms pulsar in the Vela supernova remnant [95]. The fact that these pulsars are located within supernova remnants provided striking confirmation that neutron stars are born in core collapse supernovae from massive main sequence stars. These exciting radio discoveries triggered subsequent pulsar searches at nearly all wavelengths. Since those early days of pulsar astronomy more than 1,800 radio pulsars have been discovered (see, e.g., the ATNF pulsar database [102] and Chaps. 1 and 2 in this book).

Many radio pulsars had been observed by mid-seventies, and two of them, the Crab and Vela pulsars, had been detected at high photon energies. Although the interpretation of both isolated and accreting pulsars as neutron stars with enormous magnetic fields, $\sim 10^{12}$ G, had been generally accepted, no direct evidence on the existence of such huge fields had been obtained. This evidence came from a remarkable spectral observation of Hercules X-1, an accreting binary pulsar discovered with *Uhuru*. On May 3, 1976, a team of the Max-Planck Institut für extraterrestrische Physik in Garching and the Astronomische Institut of the University of Tübingen, led by Joachim Trümper, launched from Palestine (Texas) a balloon experiment, equipped with a collimated NaI scintillation counter and a NaI–CsI-phoswich detector, sensitive in the range 15–160 keV. They easily detected the 1.24 s pulsations up to 80 keV [93]. However, when Bruno Sacco and Wolfgang Pietsch attempted to fit the observed spectrum with usual continuum spectral models, they found that a one-component continuum model cannot represent the data – all fits gave unacceptably large residuals at ~40–60 keV. Further data analysis confirmed

---

[3] When a charged relativistic particle moves along a curved magnetic field line, it is accelerated transversely and radiates. This *curvature radiation* is closely related to *synchrotron radiation* caused by gyration of particles around the magnetic field lines.

that the spectral feature was not an artifact (e.g., due to incomplete shielding of the in-flight calibration source ^{241}Am, which emitted a spectral line at $E = 59.5\,\mathrm{keV}$). It was Joachim Trümper who first recognized that the excess emission at 58 keV (or an absorption feature at 42 keV, depending on interpretation – cf. Fig. 6.1) could be associated with the resonant electron cyclotron emission or absorption in the hot polar plasma of the rotating neutron star. The corresponding magnetic field strength would then be 6×10^{12} or 4×10^{12} G [152]. This observation provided the first direct measurement of a neutron star magnetic field and confirmed the basic theoretical predictions that neutron stars are highly magnetized, fast spinning compact objects.

Particularly important results on isolated neutron stars, among many other X-ray sources, were obtained with *HEAO-2*, widely known as the *Einstein* X-ray observatory. *Einstein* investigated the soft X-ray radiation from the previously known Crab and Vela pulsars and resolved the compact nebula around the Crab pulsar [2]. It discovered pulsed X-ray emission from two more very young pulsars, PSR B0540−69 in the Large Magellanic Cloud and PSR B1509−58, having periods of 50 and 150 ms, respectively. Interestingly, these pulsars were the

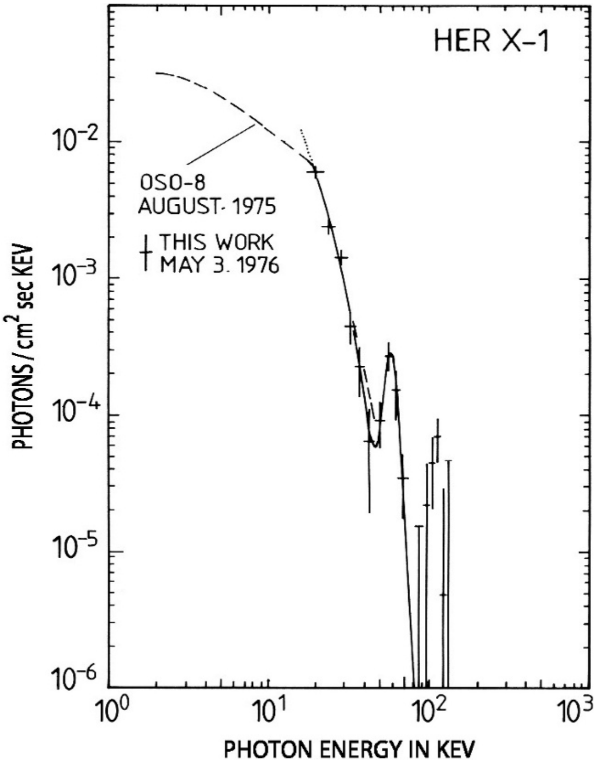

Fig. 6.1 Unfolded X-ray spectrum from Hercules X-1, showing the first measurement of a cyclotron line in a pulsed spectrum of an accreting neutron star. Image from [152]

first ones to be discovered in the X-ray band and only subsequently at radio frequencies. *Einstein* also detected X-rays from three middle-aged radio pulsars, PSR B0656+14, B1055−52, B1951+32 and the X-ray counterparts of two nearby old radio pulsars, PSR B0950+08 and B1929+10. In addition, many supernova remnants were mapped – 47 in our Galaxy and 10 in the Magellanic Clouds and several neutron star candidates were detected as faint, soft point sources close to the center of the supernova remnants RCW 103, PKS 1209−51/52, Puppis-A and Kes 73.

Some additional information on isolated neutron stars was obtained by *EXOSAT* (*European X-ray Observatory Satellite*). In particular, it measured the soft X-ray spectra of the middle-aged pulsar PSR B1055−52 and of a few neutron star candidates in supernova remnants (e.g., PKS 1209−51/52).

The situation improved drastically in the 1990s due to the results from ROSAT, ASCA, EUVE, BeppoSAX and RXTE, as well as Chandra and XMM-Newton launched close to the millennium. The complement to ROSAT, covering the harder X-ray band 1–10 keV, was *ASCA* launched in 1993. The *EUVE* (*Extreme Ultraviolet Explorer*) was launched in 1992 and was sensitive in the range 70–760 RA. It was able to observe several neutron stars at very soft X-rays, 0.07–0.2 keV. The contributions to neutron star research, provided by the instruments aboard *BeppoSAX*, sensitive in the range of 0.1–200 keV, and *RXTE* (*Rossi X-ray Timing Explorer*), both launched in the mid-1990s, were particularly useful for studying X-ray binaries, including accretion-powered pulsars.

At present *Chandra*, with its outstanding sub-arcsecond imaging capability and *XMM-Newton* with its unprecedently high spectral sensitivity and collecting power provide excellent new data.

In the following we will summarize the result on the X-ray emission properties of neutron stars based on observations with these missions. We will browse through the various categories from young Crab-like pulsars to very old radio pulsars, including recycled millisecond pulsars as well as neutron stars showing pure thermal emission. Before doing so, however, we will briefly review the various emission processes discussed to be the source for their observed X-ray emission.

6.2 Physics and Astrophysics of Isolated Neutron Stars

Neutron stars represent unique astrophysical laboratories which allow us to explore the properties of matter under the most extreme conditions observable in nature.[4] Studying neutron stars is therefore an interdisciplinary field, where astronomers and astrophysicists work together with a broad community of physicists. Particle, nuclear and solid-state physicists are strongly interested in the internal structure of neutron stars which is determined by the behavior of matter at densities above the nuclear density $\rho_{\mathrm{nuc}} = 2.8 \times 10^{14}\mathrm{g\ cm}^{-3}$. Plasma physicists are modeling the pulsar emission mechanisms using electrodynamics and general relativity. It is beyond the

---

[4] Although black holes are even more compact than neutron stars, they can only be observed through the interaction with their surroundings.

scope of this article to describe in detail the current status of the theory of neutron star structure or the magnetospheric emission models. We rather refer the reader to the literature [21, 23, 53, 108, 158] and provide only the basic theoretical background relevant to Sect. 6.3 which summarizes the observed high-energy emission properties of rotation-powered pulsars and radio-quiet neutron stars.

6.2.1 Rotation-Powered Pulsars: The Magnetic Braking Model

Following the ideas of Pacini [120, 121] and Gold [54, 55] the more than 1,800 radio pulsars detected so far can be interpreted as rapidly spinning, strongly magnetized neutron stars radiating at the expense of their rotational energy. This very useful concept allows one to obtain a wealth of information on basic neutron star/pulsar parameters just from measuring the pulsar's period and period derivative. Using the Crab pulsar as an example will make this more clear. A neutron star with a canonical radius of $R = 10\,\mathrm{km}$ and a mass of $M = 1.4\ \mathrm{M}_\odot$ has a moment of inertia $I \approx (2/5)MR^2 \approx 10^{45}\,\mathrm{g\,cm}^2$. The Crab pulsar spins with a period of $P = 33.403\,\mathrm{ms}$. The rotational energy of such a star is $E_{\mathrm{rot}} = 2\pi^2\, I\, P^{-2} \approx 2\times 10^{49}$ erg. This is comparable with the energy released in thermonuclear burning by a usual star over its entire live. Very soon after the discovery of the first radio pulsars it was noticed that their spin periods increase with time. For the Crab pulsar, the period derivative is $\dot P = 4.2\times 10^{-13}\,\mathrm{s\,s}^{-1}$, implying a decrease in the star's rotation energy of $\mathrm{d}E_{\mathrm{rot}}/\mathrm{d}t \equiv \dot E_{\mathrm{rot}} = -I\Omega\dot\Omega = 4\pi^2 I\dot P P^{-3} \approx 4.5\times 10^{38}\,\mathrm{erg\ s}^{-1}$. Ostriker and Gunn [117] suggested that the pulsar slow-down is due to the braking torque exerted on the neutron star by its magneto-dipole radiation, that yields $\dot E_{\mathrm{brake}} = -(32\pi^4/3c^3)\,B_\perp^2\,R^6\,P^{-4}$ for the energy loss of a rotating magnetic dipole, where $B_\perp$ is the component of the equatorial magnetic field perpendicular to the rotation axis. Equating $\dot E_{\mathrm{brake}}$ with $\dot E_{\mathrm{rot}}$, we find $B_\perp = 3.2\times 10^{19}(P\dot P)^{1/2}$ G. For the Crab pulsar, this yields $B_\perp = 3.8\times 10^{12}$ G. From $\dot E_{\mathrm{rot}} = \dot E_{\mathrm{brake}}$ one further finds that $\dot P \propto P^{-1}$, for a given $B_\perp$. This relation can be generalized as $\dot P = kP^{2-n}$, where k is a constant, and n is the so-called magnetic braking index ($n = 3$ for the magneto-dipole braking). Assuming that the initial rotation period P_0 at the time t_0 of the neutron star formation was much smaller than today, at $t = t_0 + \tau$, we obtain $\tau = P/[(n-1)\dot P]$, or $\tau = P/(2\dot P)$ for $n = 3$. This quantity is called the characteristic spin-down age. It is a measure for the time span required to lose the rotational energy $E_{\mathrm{rot}}(t_0) - E_{\mathrm{rot}}(t)$ via magneto-dipole radiation. For the Crab pulsar one finds $\tau = 1{,}258$ yrs. As the neutron star in the Crab supernova remnant is the only pulsar for which its historical age is known (the Crab supernova was observed by Chinese astronomers in 1054 AD, cf. also Sect. 6.3.1), we see that the spin-down age exceeds the true age by about 25%. Although the spin-down age is just an estimate for the true age of the pulsar, it is the only one available for pulsars other than the Crab, and it is commonly used in evolutionary studies such as, e.g., neutron star cooling (cf. Chaps. 11–12).

A plot of observed periods vs. period derivatives is shown in Fig. 6.2, using the pulsars from the ATNF online pulsar database [102]. Such a P–$\dot P$ diagram is

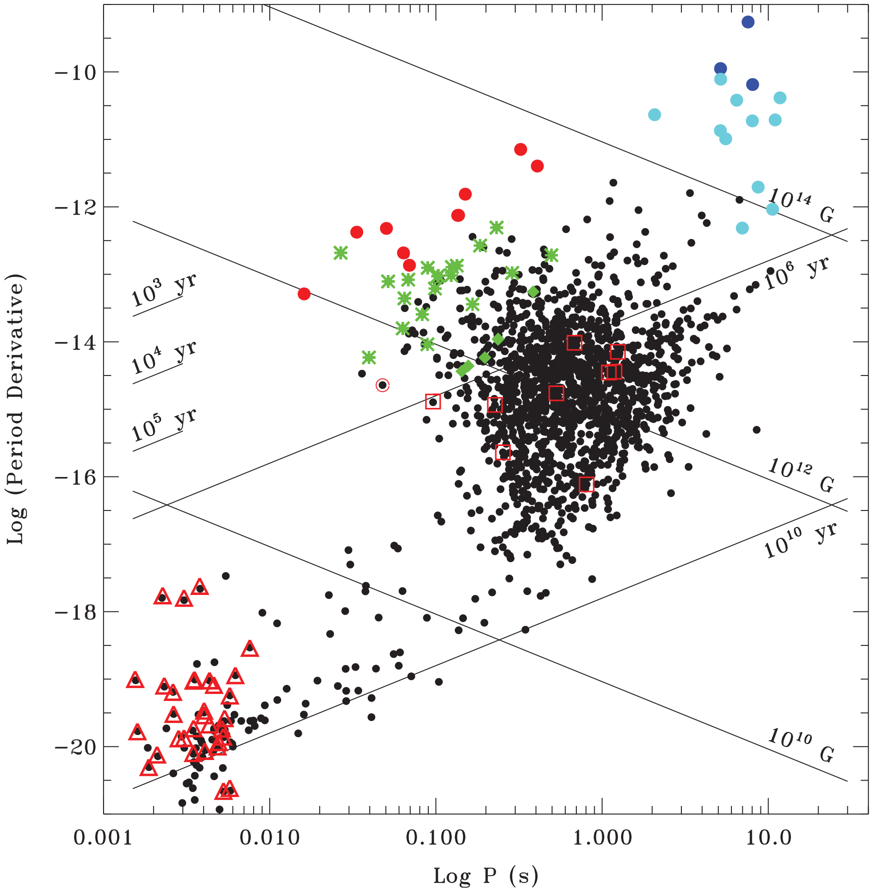

Fig. 6.2 The P–$\dot{P}$ diagram – distribution of rotation-powered pulsars (*small black dots*) over their spin parameters. The *straight lines* correspond to constant ages $\tau = P/(2\dot{P})$ and magnetic field strengths $B_\perp = 3.2 \times 10^{19}(P\dot{P})^{1/2}$ as deduced in the frame of the magnetic braking model. Separate from the majority of ordinary field pulsars are the millisecond pulsars in the lower left corner and the high magnetic field pulsars – soft gamma-ray repeaters (*dark blue*) and anomalous X-ray pulsars *light blue*) – in the *upper right*. Although magnetars and anomalous X-ray pulsars are not rotation-powered, they are included in this plot to visualize their estimated superstrong magnetic fields. X-ray detected pulsars are indicated by colored symbols. *Red filled circles* indicate the Crab-like pulsars. *Green stars* indicate Vela-like pulsars, *green diamonds* the X-ray detected cooling neutron stars, *red squares* million years old pulsars and *red triangles* the X-ray detected millisecond pulsars

extremely useful for classification purposes. The colored symbols represent those pulsars which were detected at X-ray energies by mid 2008. The objects in the upper right corner represent the soft-gamma-ray repeaters (SGRs) and anomalous X-ray pulsars (AXPs) which have been suggested to be magnetars (neutron stars with ultra strong magnetic fields).

Although the magnetic braking model is generally accepted, the *observed* spin-modulated emission, which gave pulsars their name, is found to account only for a small fraction of $\dot{E}$. The efficiencies, $\eta = L/\dot{E}$, observed in the radio and optical bands are typically in the range $\sim 10^{-7}$–10^{-5}, whereas they are about 10^{-4}–10^{-3} and $\sim 10^{-2}$–10^{-1} at X-ray and gamma-ray energies, respectively [15]. It has therefore been a long-standing question how rotation-powered pulsars lose the bulk of their rotational energy.

The fact that the energy loss of rotation-powered pulsars cannot be fully accounted for by the magneto-dipole radiation is known from the investigation of the pulsar braking index, $n = 2 - P\ddot{P}\dot{P}^{-2}$. Pure dipole radiation would imply a braking index $n = 3$, whereas the values observed so far are $n = 2.515 \pm 0.005$ for the Crab, $n = 2.8 \pm 0.2$ for PSR B1509−58, $n = 2.28 \pm 0.02$ for PSR B0540−69, 2.91 ± 0.05 for PSR J1911−6127, 2.65 ± 0.01 for PSR J1846−0258 and $n = 1.4 \pm 0.2$ for the Vela pulsar. The deviation from $n = 3$ is usually taken as evidence that a significant fraction of the pulsar's rotational energy is carried away by a pulsar wind, i.e., a mixture of charged particles and electromagnetic fields, which, if the conditions are appropriate, forms a *pulsar-wind nebula* observable at optical, radio and X-ray energies. Such pulsar-wind nebulae (often called plerions or synchrotron nebulae) are known so far *only* for a few young and powerful (high $\dot{E}$) pulsars and for some center-filled supernova remnants, in which a young neutron star is expected, but only emission from its plerion is detected.

Thus, the popular model of magnetic braking provides plausible estimates for the neutron star magnetic field $B_\perp$, its rotational energy loss $\dot{E}$, and the characteristic age τ, but it does not provide detailed information about the physical processes which operate in the pulsar magnetosphere and which are responsible for the broad-band spectrum, from the radio to the X-ray and gamma-ray bands. Forty years after the discovery of pulsars the physical details of their emission mechanisms are still barely known. As a consequence, there exist a number of magnetospheric emission models, but no generally accepted theory.

6.2.2 High-Energy Emission Models

Although rotation-powered pulsars are most widely known for their radio emission, the mechanism of the radio emission is poorly understood. However, it is certainly different from those responsible for the high-energy (infrared through gamma-ray) radiation observed from them with space observatories. It is well known that the radio emission of pulsars is a coherent process, and the coherent curvature radiation has been proposed as the most promising mechanism (see [108] and references therein). On the other hand, the optical, X-ray and gamma-ray emission observed in pulsars must be incoherent. Therefore, the fluxes in these energy bands are directly proportional to the densities of the radiating high-energy electrons in the acceleration regions, no matter which radiation process (synchrotron radiation, curvature radiation or inverse Compton scattering) is at work at a given energy. High-energy observations thus provide the key for the understanding of the pulsar emission mechanisms. So far, the high-energy radiation detected from rotation-driven pulsars has been attributed to various thermal and non-thermal emission processes including the following:

- Non-thermal emission from charged relativistic particles accelerated in the pulsar magnetosphere (cf. Fig. 6.3). As the energy distribution of these particles follows a power-law, the emission is also characterized by power-law-like spectra in broad energy bands. The emitted radiation can be observed from optical to the gamma-ray band.
- Extended emission from pulsar-driven synchrotron nebulae. Depending on the local conditions (density of the ambient interstellar medium), these nebulae can be observed from radio through hard X-ray energies.
- Photospheric emission from the hot surface of a cooling neutron star. In this case a modified black-body spectrum and smooth, low-amplitude intensity variations with the rotational period are expected, observable from the optical through the soft X-ray range.
- Thermal soft X-ray emission from the neutron star's polar caps which are heated by the bombardment of relativistic particles streaming back to the surface from the pulsar magnetosphere.

In almost all pulsars the observed X-ray emission is due to a mixture of different thermal and non-thermal processes. Often, however, the available data do not allow to fully discriminate between the different emission scenarios. This was true for ROSAT, ASCA and BeppoSAX observations of pulsars and is – at a certain level – still true in Chandra and XMM-Newton data.

In the following subsections we will briefly present the basics on the magnetospheric emission models as well as material relevant to thermal emission from the neutron star surface.

Magnetospheric Emission Models

So far, there is no consensus as to where the pulsar high-energy radiation comes from (see for example [108] and Chaps. 15, 18 and 19). There exist two main types of models – the *polar cap models*, which place the emission zone in the immediate vicinity of the neutron star's polar caps, and the *outer gap models*, in which this zone is assumed to be close to the pulsar's light cylinder[5] to prevent materializing of the photons by the one-photon pair creation in the strong magnetic field, according to $\gamma + B \rightarrow e^{+} + e^{-}$ (see Fig. 6.3). The gamma-ray emission in the polar cap models forms a hollow cone centered on the magnetic pole, producing either double-peaked or single-peaked pulse profiles, depending on the observer's line of

---

[5] The light cylinder is a virtual cylinder whose radius, $R_L = cP/(2\pi)$, is defined by the condition that the azimuthal velocity of the co-rotating magnetic field lines is equal to the speed of light.

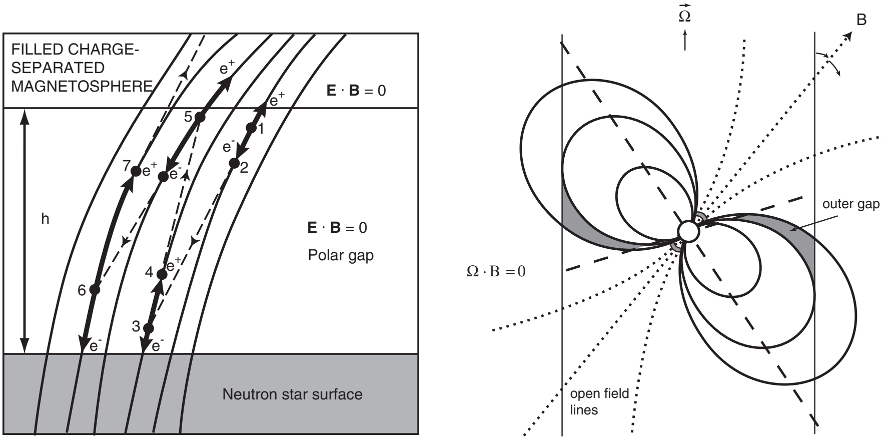

Fig. 6.3 Geometry of the acceleration zones as they are defined in the polar cap model (*left*), according to Ruderman and Sutherland [138], and outer gap model (*right*), according to Cheng, Ho and Ruderman [32, 33]. The polar cap model predicts "pencil" beams emitted by particles accelerated along the curved magnetic field lines. According to the outer gap model, the pulsar radiation is emitted in "fan" beams. Being broader, the latter can easier explain two (and more) pulse components as observed in some X-ray and gamma-ray pulsars

sight. The outer gap model was originally proposed to explain the bright gamma-ray emission from the Crab and Vela pulsars [32, 33] as the efficiency to get high-energy photons out of the high B-field regions close to the surface is rather small. Placing the gamma-ray emission zone at the light cylinder, where the magnetic field strength is reduced to $B_L = B(R/R_L)^3$, provides higher gamma-ray emissivities which are in somewhat better agreement with the observations. In both types of models, the high-energy radiation is emitted by relativistic particles accelerated in the very strong electric field, $\mathcal{E} \sim (R/cP)B$, generated by the magnetic field co-rotating with the neutron star. These particles are generated in cascade (avalanche) processes in charge-free gaps, located either above the magnetic poles or at the light cylinder. The main photon emission mechanisms are synchrotron/curvature radiation and inverse Compton scattering of soft thermal X-ray photons emitted from the hot neutron star surface.

In recent years the polar-cap and outer-gap models have been further developed, incorporating new results on gamma-ray emission from pulsars obtained with the Compton Gamma-Ray Observatory. At the present stage, the observational data can be interpreted with any of the two models, albeit under quite different assumptions on pulsar parameters. The critical observations to distinguish between the two models include, e.g., measuring the relative phases between the peaks of the pulse profiles at different energies. Probably the GLAST gamma-ray observatory (cf. Chap. 23) which is supposed to become operational in summer 2008 will provide valuable information to further constrain both models.

Thermal Evolution of Neutron Stars

Neutron stars are formed at very high temperatures, $\sim 10^{11}$ K, in the imploding cores of supernova explosions. Much of the initial thermal energy is radiated away from the interior of the star by various processes of neutrino emission (mainly, Urca processes and neutrino bremsstrahlung), leaving a one-day-old neutron star with an internal temperature of about 10^9–10^{10} K. After $\sim$100 yr (typical time of thermal relaxation), the star's interior (densities $\rho > 10^{10}\,\mathrm{g\,cm^{-3}}$) becomes nearly isothermal, and the energy balance of the cooling neutron star is determined by the following equation:

$$C(T_i)\,\frac{\mathrm{d}T_i}{\mathrm{d}t} = -L_\nu(T_i) - L_\gamma(T_s) + \sum_k H_k\,,$$

where T_i and T_s are the internal and surface temperatures, $C(T_i)$ is the heat capacity of the neutron star (cf. Chaps. 11 and 12). Neutron star cooling thus means a decrease of thermal energy, which is mainly stored in the stellar core, due to energy loss by neutrinos from the interior ($L_\nu = \int Q_\nu\,\mathrm{d}V$, Q_ν is the neutrino emissivity) plus energy loss by thermal photons from the surface ($L_\gamma = 4\pi R^2 \sigma T_s^4$). The relationship between T_s and T_i is determined by the thermal insulation of the outer envelope ($\rho < 10^{10}\,\mathrm{g\,cm^{-3}}$), where the temperature gradient is formed. The results of model calculations, assuming that the outer envelope is composed of iron, can be fitted with a simple relation

$$T_s = 3.1\,(g/10^{14}\,\mathrm{cm\,s^{-2}})^{1/4}\,(T_i/10^9\,\mathrm{K})^{0.549} \times 10^6\,\mathrm{K}\,,$$

where g is the gravitational acceleration at the neutron star surface [64]. The cooling rate might be reduced by heating mechanisms H_k, like frictional heating of superfluid neutrons in the inner neutron star crust or some exothermal nuclear reactions.

Neutrino emission from the neutron star interior is the dominant cooling process for at least the first 10^5 years. After $\sim 10^6$ years, photon emission from the neutron star surface takes over as the main cooling mechanism. The thermal evolution of a neutron star after the age of $\sim$10–100 yr, when the neutron star has cooled down to $T_s = 1.5$–3×10^6 K, can follow two different scenarios, depending on the still poorly known properties of super-dense matter (see Fig. 6.13). According to the so-called *standard cooling scenario*, the temperature decreases gradually, down to ~ 0.3–1×10^6 K, by the end of the neutrino cooling era and then falls down exponentially, becoming lower than $\sim 0.1 \times 10^6$ K in $\sim 10^7$ yr. In this scenario, the main neutrino generation processes are the modified Urca reactions, $\mathrm{n} + N \rightarrow \mathrm{p} + N + \mathrm{e} + \bar{\nu}_e$ and $\mathrm{p} + N + \mathrm{e} \rightarrow \mathrm{n} + N + \nu_e$, where N is a nucleon (neutron or proton) needed to conserve momentum of reacting particles (cf. Table 6.1). In the *accelerated cooling scenarios*, associated with higher central densities (up to $10^{15}\,\mathrm{g\,cm^{-3}}$) and/or exotic interior composition (e.g., pion condensation, quark-gluon plasma), a sharp drop of temperature, down to 0.3–0.5×10^6 K, occurs at an age of $\sim$10–100 yr, followed by a more gradual decrease, down to the same $\sim 0.1 \times 10^6$ K at $\sim 10^7$ yr. The faster cooling is caused by the direct Urca reactions, $\mathrm{n} \rightarrow \mathrm{p} + \mathrm{e} + \bar{\nu}_e$ and $\mathrm{p} + \mathrm{e} \rightarrow \mathrm{n} + \nu_e$, allowed at very high densities.

Table 6.1 Nuclear reactions and their neutrino emissivity as a function of neutron star temperature [123]. T_9 is the temperature in units of 10^9 K. Each particle (n, p, e^-) which takes part in a reaction contributes to the temperature dependence with a T and each neutrino with a T^3. The reactions denoted as direct-Urca, π-condensate, Quark-URCA-process and Kaon condensate are taken into account in the so-called accelerated cooling models. They have an order of magnitude higher neutrino emissivity in comparison with the other nuclear reactions. The higher the neutrino emissivity is the more efficient is the neutron star cooling.

Neutrino emissivity used in neutron star cooling models		
Process	Nuclear reaction	Emissivity (erg/s/cm^3)
Direct URCA-process	$\mathrm{n} \rightarrow \mathrm{p} + \mathrm{e}^- + \bar{\nu}_e$ $\mathrm{p} + \mathrm{e}^- \rightarrow \mathrm{n} + \nu_e$	$\sim 10^{27} \times T_9^6$
π-Condensate	$\mathrm{n} + \pi^- \rightarrow \mathrm{n} + \mathrm{e}^- + \bar{\nu}_e$ $\mathrm{n} + \mathrm{e}^- \rightarrow \mathrm{n} + \pi^- + \nu_e$	$\sim 10^{26} \times T_9^6$
Quark-URCA-process	$d \rightarrow u + \mathrm{e}^- + \bar{\nu}_e$ $u + \mathrm{e}^- \rightarrow d + \nu_e$	$\sim 10^{26}\ \alpha_c\ T_9^6$
Kaon condensate	$\mathrm{n} + K^- \rightarrow \mathrm{n} + \mathrm{e}^- + \bar{\nu}_e$ $\mathrm{n} + \mathrm{e}^- \rightarrow \mathrm{n} + K^- + \nu_e$	$\sim 10^{25} \times T_9^6$
Modified URCA-process	$\mathrm{n} + \mathrm{n} \rightarrow \mathrm{n} + \mathrm{p} + \mathrm{e}^- + \bar{\nu}_e$ $\mathrm{n} + \mathrm{p} + \mathrm{e}^- \rightarrow \mathrm{n} + \mathrm{n} + \nu_e$	$\sim 10^{21} \times T_9^8$
Direct coupled Electron–Neutrino-process	$\gamma + \mathrm{e}^- \rightarrow \mathrm{e}^- + \nu_e + \bar{\nu}_e$ $\gamma_{plasmon} \rightarrow \nu_e + \bar{\nu}_e$ $\mathrm{e}^+ + \mathrm{e}^- \rightarrow \nu_e + \bar{\nu}_e$	$\sim 10^{20} \times T_9^8$
Neutron–Neutron and Neutron–Proton-Bremsstrahlung	$\mathrm{n} + \mathrm{n} \rightarrow \mathrm{n} + \mathrm{n} + \nu + \bar{\nu}$ $\mathrm{n} + \mathrm{p} \rightarrow \mathrm{n} + \mathrm{p} + \nu + \bar{\nu}$	$\sim 10^{19} \times T_9^8$
Electron–Ion–Neutrino-Bremsstrahlung	$\mathrm{e}^- + (Z,A) \rightarrow$ $\mathrm{e}^- + (Z,A) + \nu_e + \bar{\nu}_e$	$\propto T_9^6$

The neutron star models used in these calculations are based on a *moderate* equation of state which opens the direct Urca process for $M > 1.35\,M_\odot$, the stars with lower M undergo the standard cooling. Recent studies have shown that both the standard and accelerated cooling can be substantially affected by nucleon superfluidity in the stellar interiors (see [122, 153, 163] for comprehensive reviews). In particular, many cooling curves exist intermediate between those of the standard and accelerated scenarios, depending on the properties of nucleon superfluidity, which are also poorly known.

Thus, the thermal evolution of neutron stars is very sensitive to the composition and structure of their interiors, in particular, to the equation of state at supernuclear densities. Therefore, measuring surface temperatures of neutron stars is an important tool to study super-dense matter. Since typical temperatures of such neutron stars correspond to the extreme UV – soft X-ray range, the thermal radiation from cooling neutron stars can be observed with X-ray detectors sufficiently sensitive at $E \lesssim 1\,\mathrm{keV}$.

6.3 High-Energy Emission Properties of Neutron Stars

As a result of observations with the satellite observatories Einstein, ROSAT, ASCA, BeppoSAX, Chandra and XMM-Newton, 89 rotation-powered pulsars were detected at X-ray energies by mid 2008 (cf. Tables 6.8 and 6.9). Thus, in nearly ten years of operation XMM-Newton and Chandra have almost tripled the number of detected X-ray pulsars compared to what was known at the end of the ROSAT mission in February 1999 [13]. Table 6.2 reflects the progress made in recent years in detecting pulsars of various categories at X-ray energies. This progress clearly goes along with the increase of sensitivity and angular resolution of the available X-ray observatories. While XMM-Newton with its super collecting power allows to obtain timing and spectral information even from faint and millions of years old pulsars, Chandra stands for sub-arcsecond angular resolution which made it possible to detected and study neutron stars located in source confused regions such as supernova remnants and globular clusters.

Fortunately, with the increase in sensitivity of todays observatories a growing number of neutron stars are detected in more than just one waveband (e.g., at radio, optical, EUV, X- and gamma-rays), making it possible for the first time to carry out multi-wavelength studies of the pulsar emission. This is a big advantage as the physical processes which are responsible for the emission in different wavelength bands are obviously related to each other. Multiwavelength studies thus provide a much broader view into the physical processes operating in the neutron star magnetosphere than interpreting emission properties observed in a single wave band only.

6.3.1 *Young Neutron Stars in Supernova Remnants*

X-ray observations allow us to find both supernova remnants (SNRs) and the compact objects that may reside within them. In fact, neutron stars and neutron star

Table 6.2 Progress in detecting rotation-powered pulsars with X-ray observatories. Status as of July 2008. While EINSTEIN had only the sensitivity to see pulsed X-ray emission from the youngest and brightest pulsars and to detect a few others at the limit of its sensitivity, ROSAT/ASCA and XMM-Newton/Chandra allowed for the first time to study the emission mechanisms of rotation-powered pulsars based on a broader sample and of various categories.

Pulsar age (years)	Pulsar category	Einstein	ROSAT ASCA	XMM-Newton Chandra
$\leq 10^4$	Crab-like	3	5	9
10^4–10^5	Vela-like	1	9	22
10^5–10^6	Cooling NS		5	6
10^6–10^8	Old and nearby	1	3	9
	binary		1	1
$\geq 10^8$	ms-Pulsar		11	42
	Σ detected:	5	33	89

candidates have been found in a small fraction of the 265 known galactic SNRs [61].[6] About 38 of these compact stellar remnants in SNRs are radio pulsars, others are radio-silent (or, at least, radio-quiet) neutron stars which were found as faint point-like X-ray sources near to the geometrical center of their supernova remnant (cf. section "Central Compact Objects in Supernova Remnants").

Being in orbit for more than 80% of their nominal lifetime almost all young radio pulsars have been observed and detected by either XMM-Newton and/or Chandra (cf. Fig. 6.2). The young rotation-powered pulsars can be divided in two groups, Crab-like and Vela-like pulsars, according to somewhat different observational manifestations apparently associated with the evolution of pulsar properties with age. The radio-silent neutron stars include anomalous X-ray pulsars (AXPs), soft gamma-ray repeaters (SGRs), and "quiescent" neutron star candidates in SNRs (called Central Compact Objects, CCOs). Transient radio emission was seen from few AXPs recently [27, 101]. There is growing evidence that AXPs and SGRs are indeed magnetars (see Chap. 21 and [162] for a review). Magnetars are neutron stars with an ultra strong magnetic field ($B \geq 10^{14}$ G) which is supposed to be the source of the detected high energy radiation. A common property of these objects is that their periods are in a narrow range of 5–12 s, substantially exceeding typical periods of radio pulsars. While no gamma-ray emission has been detected from AXPs, SGRs occasionally emit soft gamma-ray bursts of enormous energy (up to 10^{42}–10^{44} erg), a property, which gave this sources their name.

Crab- and Vela-Like Pulsars

On July 4, 1054 AD, Chinese astronomers noted a *guest star* in the constellation Taurus. As we know today, this event marked the arrival of light from the death of a massive main sequence star which underwent a core collapse when its internal thermal energy produced by the nuclear fusion processes was not sufficient anymore to counteract the gravitational force against the star's collapse. The cloud of gas which we observe today at the position of this *guest star* is the Crab supernova remnant. In the optical band the nebula has an extent of 4×6 arcmin, corresponding to $\sim 7 \times 10$ light years for a distance of 2 kpc.

What we observe from the Crab nebula in X-rays is not the thermal emission from the ejecta-driven blast wave of the supernova, though, but the emission from charged particles which emit synchrotron radiation as they move along magnetic field lines. In X-rays the nebula has the form of a torus with jets, wisps and a counter-jet, having an overall extent of 2×2 arcmin in the sky. For the 2 kpc distance the radius of the torus is 0.38 pc, that of the inner ring is 0.14 pc [159]. In a series of Chandra and HST monitoring observations it was found that the nebula near to the pulsar shows temporal variability on time scales of days to weeks and month [72] (cf. also Chaps. 15 and 16). An image showing the Crab nebula and pulsar as observed by Chandra's Low Energy Transmission Grating detector is shown in Fig. 6.4.

---

[6] http://www.mrao.cam.ac.uk/surveys/snrs/ .

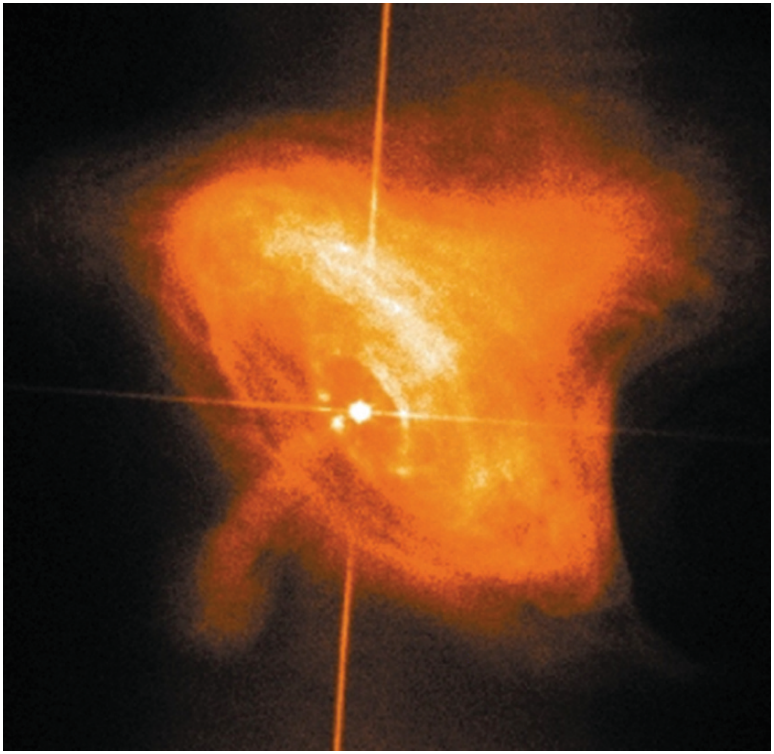

Fig. 6.4 The Crab nebula and its central pulsar as observed by the Chandra LETG detector. The cross-like feature is an artefact from the spectrum dispersed by the LETG fine-support bars

In studying this system it became clear very early that the observed non-thermal emission required a continuous input of energetic charged particles to keep the nebula emitting. It was the question of the Crab nebula's central engine which caused Pacini [120] a few month before the discovery of radio pulsars to propose that a fast spinning and strongly magnetized neutron star could be the required source which supplies the energy into the nebula.

Indeed, the 33-ms pulsar in the Crab supernova remnant, PSR B0531+21, was the first rotation-powered pulsar from which high energy radiation was detected. Being the strongest rotation-powered pulsar with the highest spin-down energy it was considered – until recent years – to be the prototype for all young neutron stars of age 10^3–10^4 years. Because of this and its favorable brightness it was studied in all frequency bands and by almost every observatory suitable to do so. The pulsar's characteristic double peaked pulse profile and its energy spectrum have been measured in detail throughout almost the entire electromagnetic spectrum. A compilation of pulse profiles as observed from the radio to the X-ray bands is shown in Fig. 6.5.

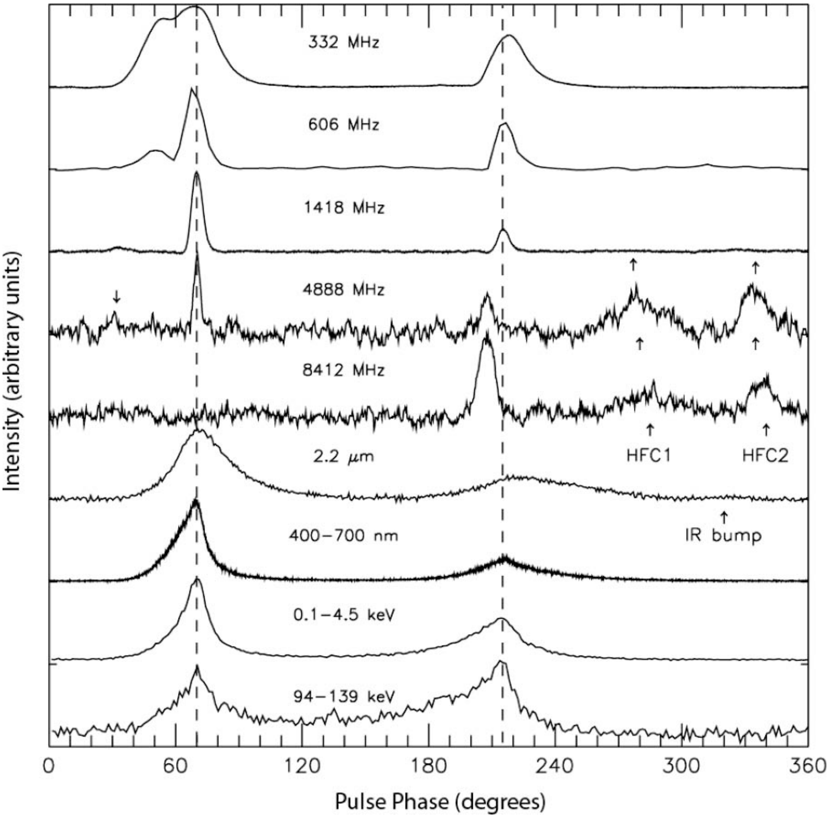

Fig. 6.5 The Crab pulsar's characteristic pulse profiles as observed at various frequency bands (from [111]). The phases of low (LFC) and high frequence (HFC) radio pulse components are indicated. The *dashed lines* indicate the phase of the main pulse component and the interpulse. The profiles have been arbitrarily aligned by the peak of the main pulse

Despite this strong interest and a wealth of data which have been taken from the pulsar since its discovery, it only recently became clear in deep Chandra observations that the X-ray emission from the Crab pulsar is actually 100% pulsed [149] and that the radio, optical and X-ray pulses are not fully phase aligned as suggested by high-energy emission models. Indeed, the X-ray pulses lead the optical pulses by the small amount of $\sim$68 µs and the optical the radio pulses by 236 µs (cf. Fig. 6.6). Mapping these pulse arrival time differences to photon travel-time differences means that for X-ray and optical pulses the arrival time delay can correspond to a difference in emission heights of 50–100 km.

As far as the pulsar's emission mechanisms are concerned, it is very well established that magnetospheric emission from charged particles, accelerated in the neutron star magnetosphere along the curved magnetic field lines, dominates the radiation not only from the Crab pulsar but from almost all young rotation-powered pulsars with ages $\lesssim 5,000$ years (cf. Sect. 6.2.2). Accordingly, the radiation

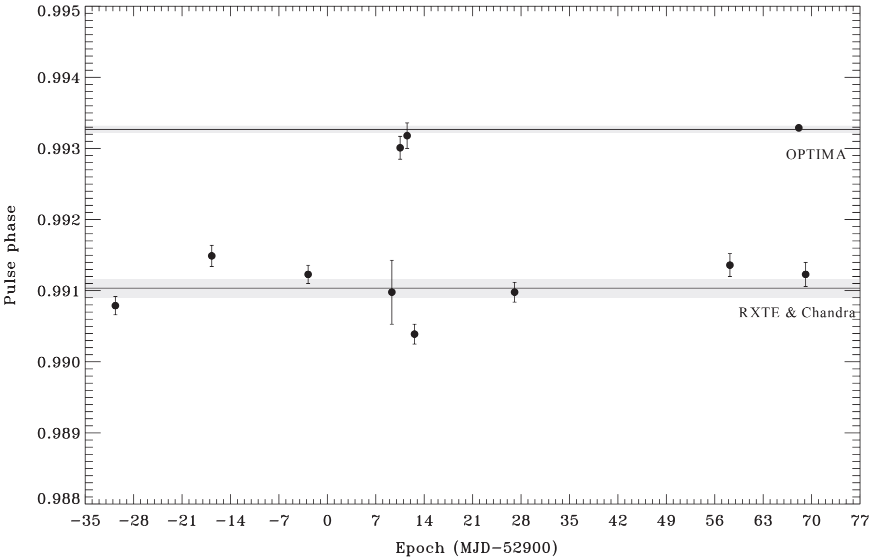

Fig. 6.6 Phase difference of the Crab pulsar's first pulse peak observed at optical and X-ray energies by OPTIMA and RXTE/Chandra. (From [5])

of Crab-like pulsars is characterized by a power-law spectrum, $\mathrm{d}N/\mathrm{d}E \propto E^{-\alpha}$, in which α is called photon-index. This implies that the energy distribution of the charged particles emitting this radiation also follows a power-law in a broad energy range. For the Crab pulsar the slope of its photon energy spectrum slowly increases with photon energy – the photon index varies from $\alpha = 1.6$ at $E \sim 1$ keV to $\alpha = 2.1$ at $E \sim 10^{10}$ eV.

Besides the Crab several other young pulsars have been studied in deep Chandra and XMM-Newton observations. Two pulsars remarkable for their rather hard X-ray spectra are PSR J1617−5055 and PSR J1811−1959 [12, 85]. PSR J1617−5055 is a 69-ms pulsar located about 7 arcmin outside the boundary of the young supernova remnant RCW 103 (cf. Fig. 6.7). The spin-down age of the pulsar is $\tau \sim 8,000$ years (cf. Table 6.8) placing it among the youngest known radio pulsars. An association of the remnant RCW 103 and the pulsar was discussed but found to be unlikely [45,92]. The pulsar distance is not very well constrained. The radio dispersion measure yields a distance of 6.1–6.9 kpc [38] but it was conclude from a comparison between dispersion measure based distances and distances obtained from HI absorption measurements of PSR 1641−45 and PSR 1718−35 – which are both located within 20^{o} of PSR J1617−5055 – that the pulsar could be as close as ~4.5 kpc [92]. PSR J1617−5055 was discovered by its X-ray pulses in archival GINGA data [151]. XMM-Newton observations classified the pulsar emission as non-thermal [12], with a rather flat photon-index of $\alpha = 1.1$–1.4 (cf. Table 6.6). The pulsar emission turns out to be highly absorbed, prohibiting any measurement of the softer cooling emission from the neutron star surface. Strong pulsed emission up to 15 keV was

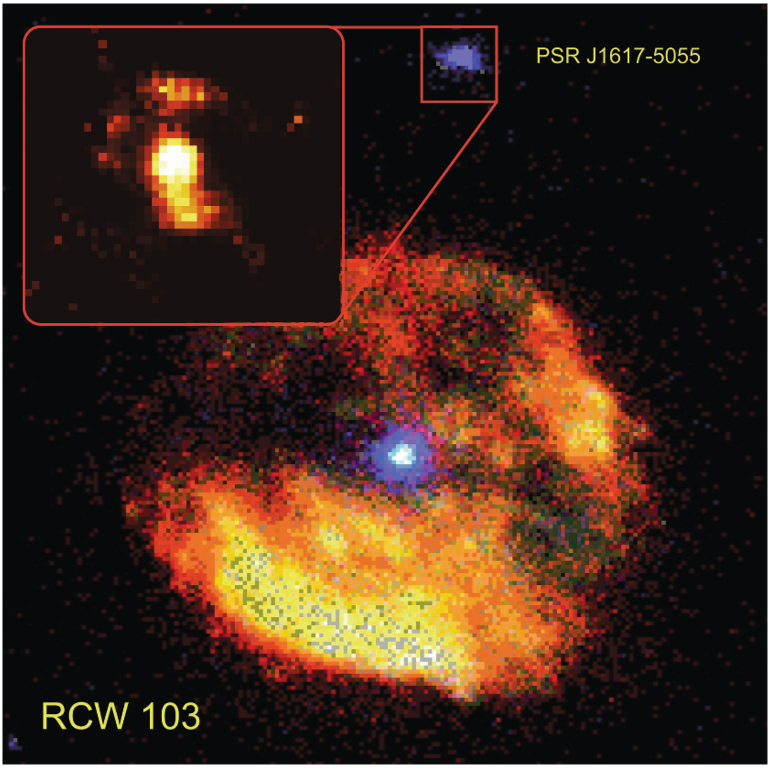

Fig. 6.7 X-ray view of RCW 103 and the young pulsar PSR J1617−5055 as observed by XMM-Newton and Chandra, respectively. The central source in RCW 103 is the CCO 1E 1613−5055. The zoomed in Chandra image on the *upper left* shows the plerion surrounding PSR J1617−5055. (RCW 103 image from [12], PSR J1617−5055 *inset* from [85])

detected by XMM-Newton [12]. The X-ray pulse profile shown in Fig. 6.8 is single peaked and shows a cross similarity to the radio profile. The pulsed fraction is at the level of 50%.

Only recently a pulsar was detected which seems to contradict this empirical evidence of non-thermal dominated emission in young rotation-powered pulsars. PSR J1119−6127, which is located in the SNR G292.2−0.5, has an age of ∼1,600 yrs and a deduced magnetic field strength of $B \sim 4.1 \times 10^{13}$ G. The latter is close to the quantum critical field of $B_{QED} = m_e^2 c^3/e\hbar = 4.4 \times 10^{13}$ G and close to the magnetar range. There is strong evidence that its spectrum is dominated by thermal radiation corresponding to a temperature of $\sim 2.4 \times 10^6$ K and an emitting radius of ∼2.7 km while its pulsed fraction in the 0.5–2.0 keV band is as high as ∼74 ± 14% [57, 140]. PSR J1119−6127 thus is the youngest pulsar for which thermal emission is detected. It is an interesting question of whether the presence of the strong magnetic field causes the completely different emission scenario than observed in other young and Crab-like pulsars. A synchrotron nebula surrounding

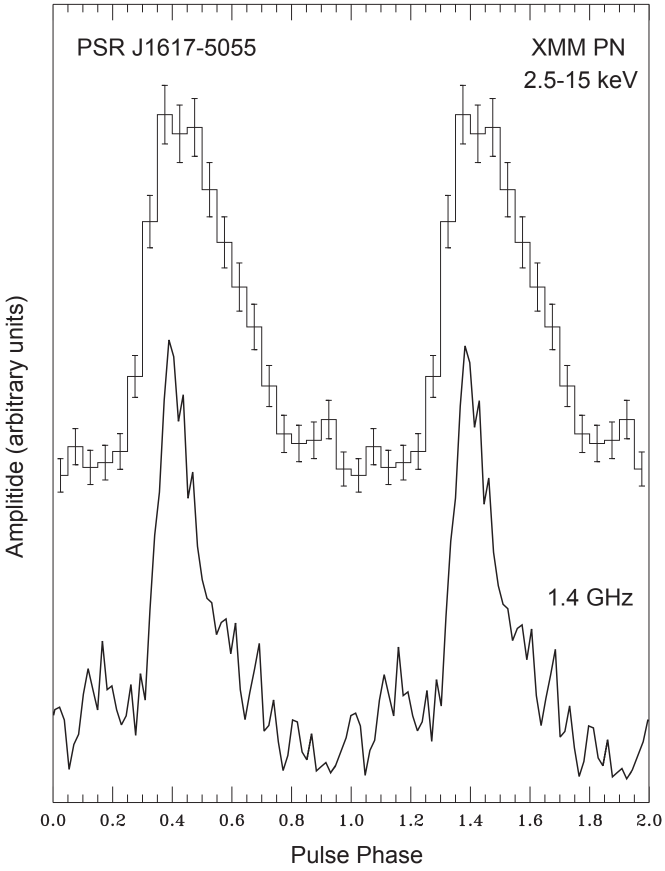

Fig. 6.8 X-ray and radio pulse profiles of PSR J1617−5055 as observed in the 2.5–15 keV band with the XMM-Newton and at 1.4 GHz with the Parkes Radio Telescope. The X-ray pulse has a duty cycle of ∼50% in the 2.5–15 keV band. Two pulse cycles are shown for clarity. Radio pulse profile from [92]

the pulsar has been detected recently above 2 keV and consists of jet-like structures extending to at least 7 arcsec from the pulsar [140]. At least from this point of few the pulsar seems to fit to the emission properties seen in other pulsars of this age.

Pulsars with a spin-down age of $\sim 10^4$–10^5 years are often referred to as Vela-like pulsars, because of their apparent similar emission properties. Among the 22 pulsars of this group which have been detected in X-rays, five of them (the Vela pulsar PSR B0833−45, PSRs J2229+6114, B1706−44, B1046−58 and B1951+32) were detected with the EGRET Gamma-ray observatory, and only the Vela pulsar has been detected in the optical band. In some respects, these objects appear to be different from the Crab-like pulsars. In particular, their optical radiation is very faint compared to that of the very young pulsars, and the overall shape of their high-energy spectra looks different. For instance, the closest ($d \approx 250$ pc) and, hence, best-investigated Vela pulsar has an optical luminosity four orders of magnitude lower than the Crab pulsar [114], whereas its rotation energy loss is only a factor of 65 lower. Its pulse profile at various wavelength is very complex and difficult to associate with the many possible emission mechanisms [99, 103]. The pulsed fraction in the soft X-ray range, $\approx 7\%$, is much lower than that observed from Crab-like pulsars.

In contrast to the young Crab-like pulsars, the soft X-ray spectrum of the Vela pulsar has a substantial thermal contribution (cf. Table 6.6) with an apparent temperature of $\approx 10^6$ K [103, 119]. On the other hand, the spatial structure of the Vela plerion strongly resembles the inner Crab nebula – it also has a torus-like structure, an inner ring and jets (see Fig. 6.9) and shows temporal intensity variations on time scales of weeks to month [127]. The symmetry axis of the nebula, which can be interpreted as the projection of the pulsar's rotation axis onto the sky plane, is roughly co-aligned with the direction of proper motion. This is similar as observed in the Crab pulsar although the misalignment there is $26 \pm 3°$. The idea of a torus configuration formed by a shock-confined pulsar wind was first introduced by Aschenbach and Brinkmann [2] as a model to explain the shape of the inner Crab

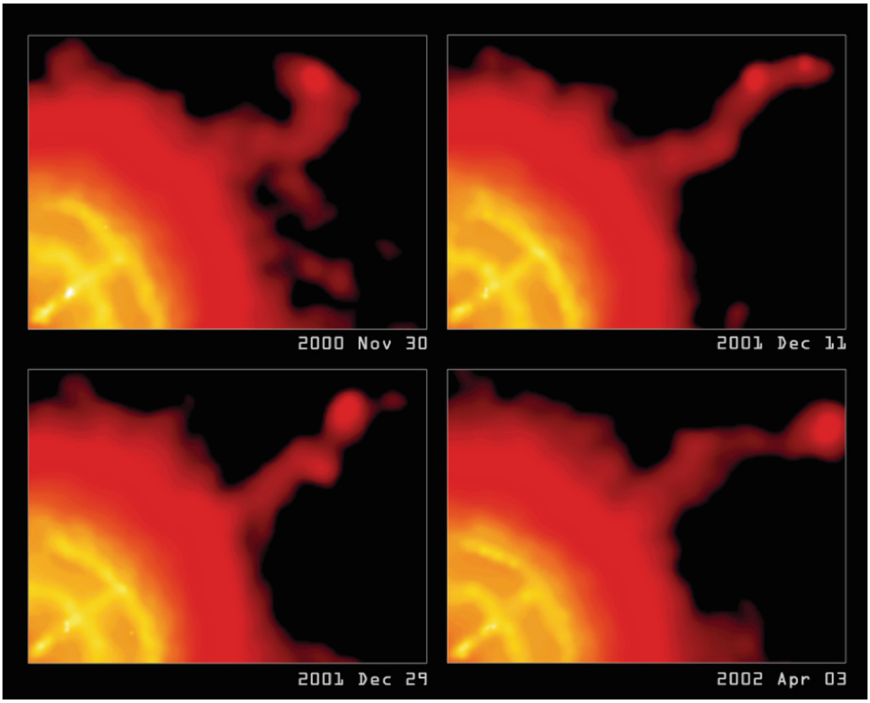

Fig. 6.9 The Vela pulsar and its plerion as observed by the Chandra ACIS-I detector. A torus and jets are seen similar as in the Crab plerionic nebula. The symmetry axis is almost aligned to the pulsar's proper motion direction. The jets are seen to vary in form and intensity on time scales of weeks to month. (Courtesy NASA/CXC/PSU/ [127])

nebula. The discovery of a similar torus-like structure in the Vela synchrotron nebula indicated that this model may be applicable to many young pulsars. According to this model, the torus-like structure and its geometrical orientation with respect to the direction of the pulsar's proper motion arise because the interaction of the post-shock plasma with the ambient medium compresses the plasma and amplifies the magnetic field ahead of the moving pulsar. This, in turn, leads to enhanced synchrotron emission with the observed torus-like shape [143].

Thus, young rotation-powered pulsars are in general surrounded by pulsar-powered nebulae (plerions) and/or supernova ejecta. The pulsar wind nebulae have been seen to show variable emission features on time scales of days to weeks and month [72, 127]. Presumably, the pulsars' magnetospheric emission extends from at least the infrared to gamma-ray energies, with typical photon indices varying between $\alpha \approx 1$–2 (cf. Tables 6.6 and 6.7). As the plerionic emission is synchrotron radiation its spectrum is a power law. In the Crab plerion Willingale et al. [161] found that the shape of the spectrum changes as a function of distance from the pulsar. He fitted the power law slope of the torus ($\alpha = 1.8 \pm 0.006$), the jet ($\alpha = 2.1 \pm 0.013$) and the outer nebula regions ($\alpha = 2.34 \pm 0.006$). Similar results were obtained by Chandra, measuring the hardness ratio distribution throughout the nebula [159]. For the pulsar, a photon spectral index of $\alpha = 1.63 \pm 0.07$ is observed (cf. Tables 6.6 and 6.7). The spectral difference between the jet and the torus is found to be likely due to an intrinsically steeper electron spectrum of the jet. The outer regions of the nebula show the steepest spectrum, which is likely to be due to enhanced synchrotron losses of the electrons during their ride from the pulsar to the outskirts.

Central Compact Objects in Supernova Remnants

For many years, it has been generally believed that all young neutron stars have similar emission properties as those observed in Crab- and Vela-like pulsars, i.e., emitting strongly pulsed radiation caused by non-thermal emission processes in the neutron star's magnetosphere. Several recent observations of compact X-ray sources in supernova remnants, however, suggest that this picture is incomplete and indeed no longer justified: it has been shown that there are other manifestations of young neutron stars, e.g., as anomalous X-ray pulsars, soft gamma-ray repeaters or simply as faint point-like X-ray source in a supernova remnant. Most of these sources were identified by their high X-ray to optical flux ratios, others simply by their locations near to the expansion centers of supernova remnants, strongly suggesting that they are indeed the compact stellar remnants formed in the supernova events. The group of SNRs which are known to host a radio-quiet but X-ray bright central compact object (CCO) is listed in Table 6.3.

Whether this group of CCOs forms a homogenous class of sources such as the rotation-powered pulsars is currently an open question and is actually difficult to answer in view of the small number of known objects. All sources in common is that (1) they are located in supernova remnants of age $\leq 10^4$ yrs, (2) their X-ray luminosi-

Table 6.3 List of X-ray detected radio-quiet and optically dim central compact objects in supernova remnants (status: mid 2008). The X-ray luminosity is computed for the energy band 0.5–10 keV and the specified distances.

CCO	Hosting SNR	Age (kyr)	d (kpc)	P	$\log L_x$ ($\mathrm{erg\,s^{-1}}$)	Ref.
CXO J232327.8+584842	Cas-A	$\sim$0.3	$\sim$3.4	…	$\sim$32.94	[47, 147]
CXO J085201.4−461753	Vela-Jr	$\sim$2?	$\sim$1.0?	…	$\sim$32.40	[3, 88]
RX J0822−4300	Pupis-A	$\sim$2	$\sim$2.2	0.22[a] s	$\sim$33.71	[80, 130]
1E 1207.4−5209	PKS 1209−51/52	$\sim$10	$\sim$2.0	0.424 s	$\sim$33.12	[59, 69]
CXO J185238.6+004020	Kes 79	$\sim$9	$\sim$7.1	0.105 s	$\sim$33.48	[58, 141]
RX J1713.7−3946	G347.3−0.5	$\sim$10	$\sim$1.0	…	$\sim$32.78	[96, 131]
1E 1613−5055	RCW 103	$\sim$2	$\sim$3.3	6.67 h	Variable	[42, 154]

[a] The periodicity of RX J0822−4300 awaits confirmation.

Table 6.4 Spectral parameters from double-blackbody fits to the CCOs in CAS-A (CXOU J232327.8+584842), Vela-Jr (CXOU J085201.4−461753), Puppis-A (RX J0822−4300), PKS 1209−51/52 (1E 1207.4−5209), Kes 79 (CXOU J185238.6+004020), G347.3−0.5 (RX J1713.7−3946) and RCW 103 (1E 1613−5055). Status mid 2008. The unabsorbed X-ray flux is computed for the energy band 0.5–10 keV. The radii of the projected emitting areas are computed for the distances specified in Table 6.3. Errors correspond to a $1-\sigma$ confidence interval.

CCO in SNR	$N_h/10^{21}$ ($\mathrm{cm^{-2}}$)	$T_1/10^6$ (K)	R_1 (km)	$T_2/10^6$ (K)	R_2 (km)	$f_x/10^{-12}$ (erg/cm/s)	Ref.
Cas-A	$12.5^{+0.3}_{-0.3}$	$4.89^{+0.07}_{-0.07}$	$0.83^{+0.03}_{-0.03}$			6.30	[67]
Vela-Jr	$3.8^{+0.4}_{-0.3}$	$4.0^{+0.3}_{-0.5}$	$0.36^{+0.05}_{-0.03}$	$6.6^{+3.1}_{-1.2}$	$0.06^{+0.06}_{-0.04}$	2.11	[7]
Pupis-A	$4.5^{+0.5}_{-0.4}$	$2.6^{+0.3}_{-0.3}$	$3.3^{+1.1}_{-0.7}$	$5.1^{+0.3}_{-0.2}$	$0.75^{+0.12}_{-0.15}$	8.94	[80]
PKS 1209−51/52	$1.0^{+0.1}_{-0.1}$	$1.92^{+0.03}_{-0.03}$	$4.5^{+0.1}_{-0.1}$	$3.7^{+0.02}_{-0.02}$	$0.83^{+0.03}_{-0.03}$	2.78	[44]
Kes 79	14^{+3}_{-3}	$5.3^{+0.5}_{-0.5}$	$0.8^{+0.1}_{-0.1}$			0.51	[58]
G347.3−0.5	$4.7^{+0.3}_{-0.4}$	$6.6^{+0.8}_{-0.8}$	$0.6^{+0.9}_{-0.9}$	$3.7^{+0.23}_{-0.23}$	$0.11^{+0.05}_{-0.05}$	5.10	[30]
RCW 103	$16.5^{+1.5}_{-1.5}$	$4.6^{+0.5}_{-0.5}$	$2.3^{+0.7}_{-0.6}$	$9.1^{+0.9}_{-0.9}$	$0.35^{+0.15}_{-0.12}$	Variable	[12]

ties are all in the braked 10^{32}–$10^{33}\ \mathrm{erg\,s^{-1}}$, (3) down to an extent of ≤ 1 arcsec none of them has been seen to maintain a plerionic X-ray nebula such as the Crab, Vela or other young pulsars and (4) no radio or optical counterpart could be detected from any CCO by now.

None of these properties is distinctive enough to justify the conclusion that all these sources form an own class of objects (e.g., Geminga is radio-silent as well). Interestingly, though, is that all CCOs share very similar spectral properties and those are markedly different from what is observed in young rotation-powered pulsars. The X-ray spectra of virtually all CCOs are very well modeled by a two component blackbody model with temperatures in the range $T_{bb} = (2\text{–}7) \times 10^6$ K and sizes of the projected emitting areas at the level of $R_{bb} \sim (0.3\text{–}5)$ km (cf. Table 6.4).

The projected emitting radii are in all cases much smaller than a canonical neutron star radius, suggesting that the radiation is emitted from a small part of the neutron star surface. It is, however, by no means clear that the double-blackbody spectral model represents the correct physical description of the emission process, even this model fits the data. An alternative spectral model providing equally good fits than the double-blackbody model does consists of a blackbody plus a power law. The inferred slope of the power law component, though, is ∼4–5 which is steeper than the photon-index $\alpha = 1$–3 observed for other rotation-powered pulsars (cf. Tables 6.6 and 6.7). However, as the true nature of the CCOs and their emission mechanisms are unknown it might not be justified to use the steepness of the power law to reject these models as unphysical. Worth to mention in this context is that the spectra observed from AXPs also require a composite blackbody plus power law model to fit. Spectral parameters obtained from them are similar to what is fitted in CCO spectra [49, 107]. The only CCO for which spectral line features were observed is 1E 1207.4$-$5209 [44]. A possible interpretation of this spectral features in terms of electron cyclotron absorption at ∼0.7, ∼1.4, ∼2.1 and ∼2.8 keV yields a neutron star magnetic field of $0.6\,(1+z) \times 10^{11} G \sim 8 \times 10^{10}$ G [44]. Herein, z is the gravitational redshift which was assumed to be at the level of 25%.

Despite the common spectral emission properties there are distinct differences in the temporal emission properties of some CCOs. For 1E 1613$-$5055 a strong periodic modulation at 6.67 ± 0.03 h has been found in long XMM-Newton observations along with changes in the X-ray flux by factors 10–100. The latter lends evidence that 1E 1613$-$5055 is actually in an eccentric orbit with a low-mass star [12, 42]. Flux variability have not been observed in any of the other CCOs. Upper limits obtained by the current observatories are in the 5–10% range.

X-ray pulsations have been observed from CXOU J185238.6+004020 in Kes 79 [58] and 1E 1207.4$-$5209 in PKS 1209$-$51 [169]. CXOU J185238.6 and 1E 1207.4$-$5209 seem to have a very stable rotation period with almost no spin-down over few years [59]. The small spin-down implies that these CCOs may have a rather small magnetic field and that these sources were born with a period close to the one observed today. The latter scenario could mean that CCOs are anti-magnetars rather than magnetars. Clearly, pulsations in more CCOs need to be detected to turn this evidence in a definite conclusion.

It recently became possible to measure the proper motion of a CCO and to confirm that its back projected birth place is in agreement with the remnants explosion center, thus providing the first confirmation that CCOs are indeed the compact remnants formed in the birth event of the hosting supernova remnant. Using two Chandra data sets which span an epoch of 1,952 days Hui and Becker [81] found that the position of RX J0822$-$4300 in Puppis-A differs by 0.57 ± 0.18 arcsec, implying a proper motion of $\mu = 107 \pm 34$ mas yr^{-1} (cf. Figs. 6.10 and 6.11). For a distance of 2.2 kpc, this proper motion is equivalent to a recoil velocity of 1120 ± 360 km s^{-1}. Both the magnitude and direction of the proper motion are in agreement with the birth place of RX J0822$-$4300, being near to the optical expansion center of the supernova remnant.

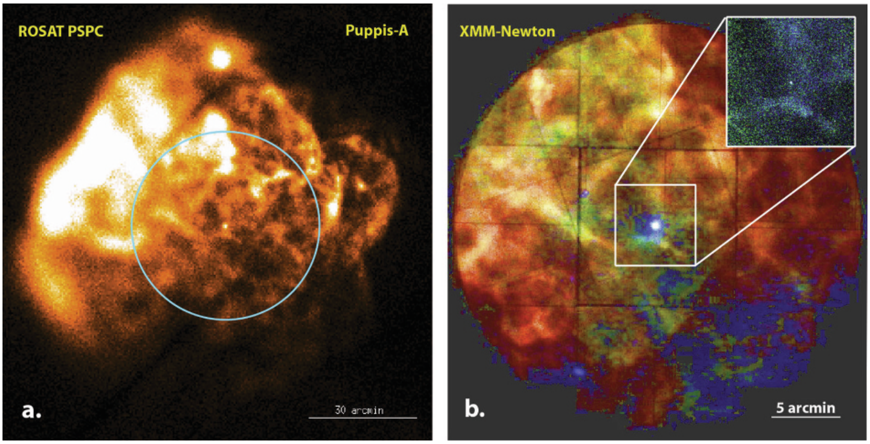

Fig. 6.10 **a** Composite ROSAT HRI image of the Puppis-A supernova remnant. The *blue ring* indicates the 30 arcmin central region which has been observed by XMM-Newton. **b** XMM-Newton MOS1/2 false color image of the central region of Puppis-A (*red*: 0.3–0.75 keV, *green*: 0.75–2 keV and *blue*: 2–10 keV). The central source is the CCO RX J0822−4300. The *inset* shows the squared region as observed by the Chandra HRC-I

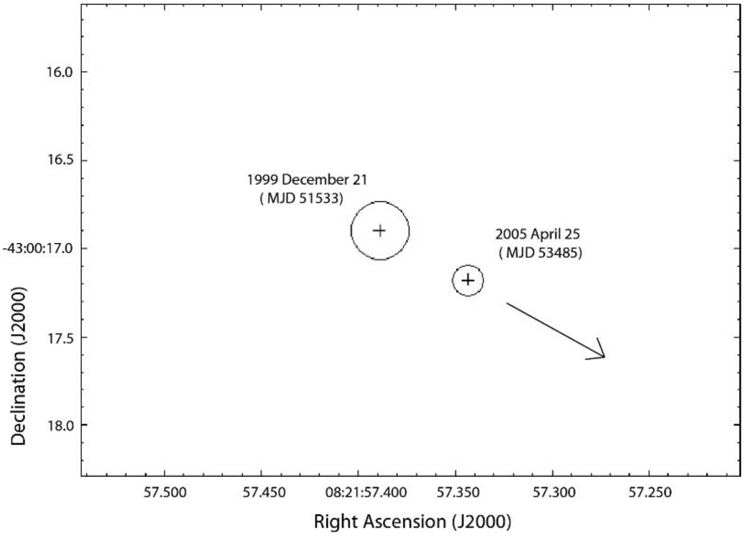

Fig. 6.11 The position (with error circle) of the cental compact object RX J0822−4300 in Puppis-A as observed by Chandra in December 1999 and April 2005. The *arrow* indicates the proper motion direction

It finally is worth to mention that, by now, the relatively small number of discovered members of this class might be to a large fraction due to observational selection effects only. From the observers point of view it is much easier to detect and identify active pulsars than these quiet compact sources observable only in the soft X-ray band. Also, once a supernova remnant disappears after about 10^5 yrs, it is almost impossible to find and identify its left over CCO. It is therefore very plausible that, in fact, CCOs may be more common than young Crab- and Vela-like radio pulsars.

6.3.2 Cooling Neutron Stars

Thermal radiation from neutron star surfaces was first detected in an unambiguous way from the Vela pulsar, PSR B0656+14, Geminga and PSR B1055−52 [118,119] using ROSAT. ROSAT also discovered seven neutron stars showing pure thermal emission in X-rays (cf. Chap. 7). More sources and many more details on spectra and temporal emission properties of cooling neutron stars were obtained with Chandra and XMM-Newton cf. [11] and Chap. 9). This data have clearly demonstrated that the soft X-ray radiation of rotation-powered pulsars in an age interval of $\sim 10^5$–10^6 yrs is dominated by thermal emission from the neutron star surface. These pulsars are apparently old enough for their magnetospheric emission to become fainter than the thermal surface emission, but they are still young and hot enough to be detectable in the soft X-ray range. As this XMM-Newton and Chandra data have shown, all middle aged pulsars for which the photon statistics is sufficient for a detailed spectral modeling require three spectral components to be modeled. This composite model includes a thermal cooling, a thermal (heated) polar-cap and a non-thermal magnetospheric emission component (cf. Fig. 6.12). The latter component is a power-law (PL) spectrum which prevails in the IR, optical, hard X-ray and gamma-ray ranges. An example fit to the IR-optical-X-ray spectrum of PSR B0656+14 is shown in Fig. 6.12.

Figure 6.13 shows a comparison of observed neutron star temperatures as a function of age compared with the results of standard cooling theory as summarized by Yakovlev and Pethick [163, 164]. For a more detailed comparison of observations and predictions from a variety of cooling models please confer Chaps. 11 and 12. Neutron star surface temperature upper limits for million years old pulsars, like PSR B1929+10, have been obtained for the first time by XMM-Newton. They are summarized in Table 6.5.

6.3.3 Old Nearby Radio Pulsars

Before the start of XMM-Newton, a consistent scenario for the evolution of the X-ray emission properties of aging rotation-powered pulsars was not available. This surprising fact was largely due to the lack of sufficient observational data. Young and middle aged neutron stars, which emit strong pulsed non-thermal and/or surface hot-spot plus cooling emission, were studied reasonably well in the X-ray band. In

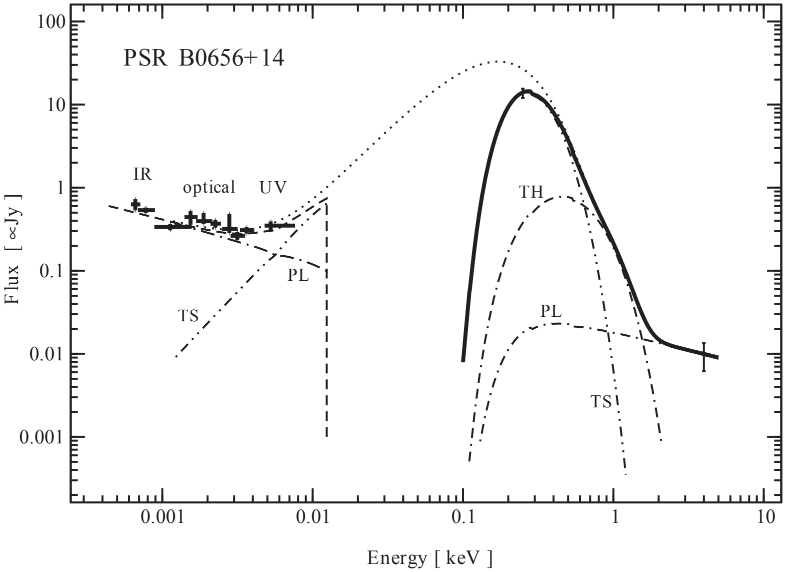

Fig. 6.12 Energy spectrum of PSR B0656+14, a prototype middle-aged cooling neutron star. Shown is the X-ray spectrum fitted with a model consisting of thermal soft (TS), thermal hard (TH) and power-law (PL) components, and IR–optical–UV fluxes measured with the HST and ground-based telescopes. The *dashed and dotted lines* show the continuation of the X-ray spectrum to the optical band with and without allowance for interstellar absorption. Figure from [13]

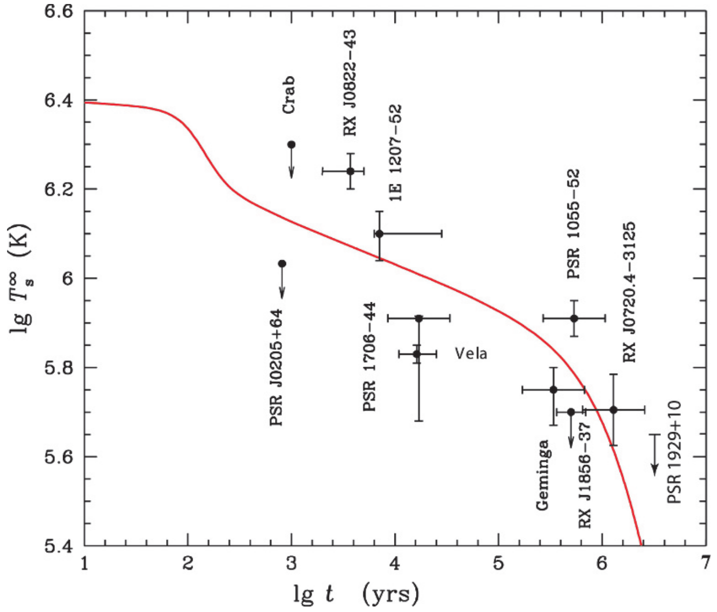

Fig. 6.13 Observations of surface temperatures and upper bounds for several isolated neutron stars. The *solid line* is the basic theoretical cooling curve of a non-superfluid neutron star with $M = 1.3\,M_\odot$ [163]. The upper limit on the temperature of the old pulsar PSR 1929+10 was added [8]

Table 6.5 3σ-Surface temperature upper limits for old non-recycled pulsars. The upper limits were obtained from adding an additional thermal component (which accounts for blackbody emission from the whole neutron star of radius $R_{NS} = 10\,\mathrm{km}$) to the best fit power law spectra. See [8–10] for details.

Pulsar	Spin-down age (10^6 years)	$3\sigma\ T_s^\infty$ (10^6 k)
B2224+65	1.12	$\leq$0.68
J2043+2740	1.20	$\leq$0.62
B0628−28	2.75	$\leq$0.53
B1929+10	3.10	$\leq$0.45
B0823+26	4.92	$\leq$0.50
B0950+08	17.5	$\leq$0.48

contrast, most old radio pulsars were too faint for a detailed examination of their X-ray emission. However, especially old rotation-powered non-recycled pulsars are of particular interest for the study of particle acceleration and high energy radiation processes near the neutron star's surface and in its magnetosphere. This is because their ages are intermediate between those of the well-studied young and cooling neutron stars, whose surface may produce copious thermal X-ray photons, and those of very old recycled millisecond pulsars, in which thermal hot-spot and non-thermal magnetospheric X-ray production mechanisms are believed to dominate.

Old, non-recycled pulsars therefore aid in answering questions such as how do the emission properties of the younger pulsars, like Geminga, PSR B0656+14 and PSR B1055−52, change as they age from $\sim 10^5$ to 10^7 years? Will the thermal emission simply fade away due to cooling with increasing age or will the star be kept hot (at about $0.5\text{–}1 \times 10^5$ K) over millions of years due to energy dissipation by processes such as internal frictional heating ($\dot{E}_{diss} \sim 10^{28}\text{–}10^{30}\,\mathrm{erg\,s^{-1}}$) and crust cracking, as proposed by vortex creeping and pinning models? What happens to the non-thermal, hard-tail emission seen in the X-ray spectra of the middle-aged field pulsars? Will this emission become the dominant source or will this component also decay with time and will only thermal emission from the hot and heated polar-caps remain?

If one extrapolates the X-ray emission properties of young and cooling neutron stars to this age bracket, one may expect that the cooling emission fades away and thermal emission from heated polar caps dominates the X-rays. Surprisingly, the X-ray emission from old pulsars is largely dominated by non-thermal radiation processes [8–10]. None of the pulsars' X-ray spectra required the inclusion of a thermal component to model the energy spectra (cf. Tables 6.6 and 6.7). Further support for an emission scenario dominated by non-thermal emission mechanisms is given by the observed temporal emission properties. The pulse profiles of PSRs B1929+10, B0950+08 and B0628−28 are not broad and sinusoidal as would have been expected for spin-modulated thermal X-ray emission from heated polar caps, but are double peaked with narrow pulse components and pulsed fractions in the range of $\sim$30–50% (cf. Fig. 6.14).

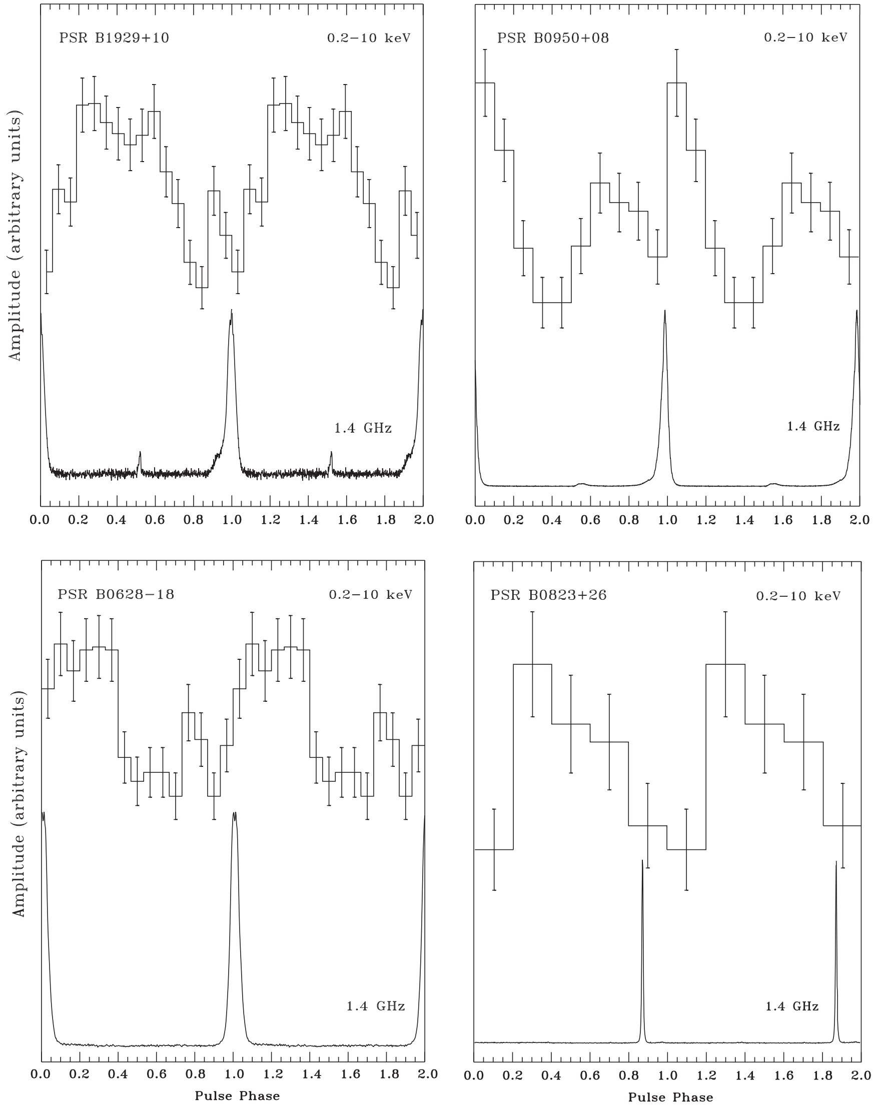

Fig. 6.14 Integrated pulse profiles of the old pulsars PSR B1929+10, B0950+08, B0628−28 and B0823+06 as observed by XMM-Newton (*top*) and at 1.4 GHz with the Effelsberg radio telescope. X-ray and radio profiles are phase aligned. Two cycles are shown for clarity. Small energy dependences in the profiles are observed for B1929+10 and B0950+08

Some models (cf. Chap. 19 and references therein) predict in the framework of the revised space-charge-limited flow model that polar cap heating, as a fraction of the spin-down luminosity, increases with pulsar age and should be most efficient for pulsars of spin-down age $\tau \sim 10^7$ yrs, if they are in fact producing pairs from curvature radiation photons. However, according to [66], PSR B0950+08 and B0823+26 cannot produce pairs from curvature radiation of primary electrons since they both lie below the curvature radiation pair death line in the P–$\dot{P}$ diagram of radio pulsars (cf. [10] for a more detailed discussion). Nevertheless, attempts have been made to fit the spectrum of PSR B0950+08 and PSR B1929+10 by including thermal models (cf. [77, 168]). By statistical means such thermal components are not required to fit the observed spectra. Therefore, contributions from heated polar caps in old pulsars have the character of upper limits rather than detections.

6.3.4 Millisecond Pulsars

In the P–$\dot{P}$ parameter space, millisecond pulsars (ms-pulsars) are distinguished from the majority of ordinary-field pulsars by their short spin periods of ≤ 20 ms and small period derivatives of $\approx 10^{-18}$–10^{-21} (cf. Fig. 6.2). In the frame of the magnetic braking model this corresponds to very old spin-down ages of typically 10^9–10^{10} years and low magnetic field strengths of $\sim 10^8$–10^{10} G. More than $\sim$75% of the known disk ms-pulsars are in binaries, usually with a low-mass white dwarf companion, compared to $\cong$1% binaries among the ordinary pulsars. This gives support to the idea that these neutron stars have been spun-up by angular momentum transfer during a past mass accretion phase [1, 4, 22]. Further evidence for this came from the discovery of seven accreting ms-pulsars which seem to confirm this scenario (see [160] for a review). Presumably, these pulsars were originally among ordinary pulsars which would have turned off because of the loss of their rotational energy if they were not in close binaries (cf. Fig. 6.15). Millisecond pulsars are therefore often called "recycled" pulsars to better distinguish them from fast spinning pulsars seen in young supernova remnants.

By mid of 2008, about 10% of the $\sim$1,800 known radio pulsars fall into the category of ms-pulsars, i.e., are recycled (cf. [102] and Chaps. 1 and 2). The majority of them (almost 137) are located in 25 globular clusters [28] which apparently provide a favorable environment for the recycling scenario. Of these globular cluster ms-pulsars 56 (41%) are solitary, the others are in binaries. Interestingly, the ratio of solitary to binary ms-pulsars is almost identical to the 40% observed in the population of galactic disk ms-pulsars. The formation of solitary recycled pulsars is not well-understood, but it is widely believed that either the pulsar's companion was evaporated (a process which is believed to be at work in the PSR 1957+20 ms-pulsar/binary system) or the system was tidally disrupted after the formation of the ms-pulsar.

Recycled pulsars had been studied exclusively in the radio domain until the 1990s, when ROSAT, ASCA, EUVE, RXTE and BeppoSAX were launched. The first millisecond pulsar discovered as pulsating X-ray source was PSR J0437−4715 [17], a nearby 5.75-ms pulsar which is in a binary orbit with a low-mass white dwarf companion. Further detections followed, which, by mid 2008 sum up to $\sim$47% of all X-ray detected rotation-powered pulsars (cf. Tables 6.8 and 6.9). The data quality available from them, though, is far from being homogenous. While from several

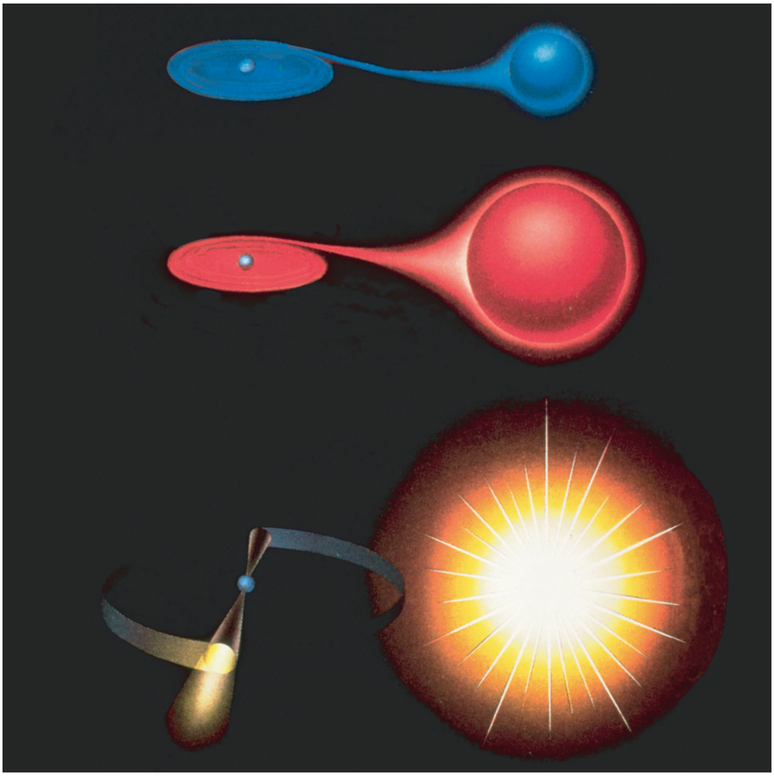

Fig. 6.15 Weakly-magnetized neutron stars that accrete matter from low-mass companion stars form the ∼150 currently known low-mass X-ray binaries (LMXBs). These systems are believed to be the progenitors of "recycled" pulsars. Along with the accretion of matter angular momentum transfer from the companion star takes place which spins-up the neutron star to millisecond periods. As the companion star evolves, a solitary ms-pulsar or a ms-pulsar binary system is left

ms-pulsars high quality spectral, temporal and spatial information is available, many others, especially those on globular clusters, are just detected with a handful of events (cf. also Chap. 8). Nevertheless, the improvements in sensitivity by Chandra and XMM-Newton provided a step forward in classifying the ms-pulsars' X-ray emission properties, indicating that there is a dichotomy between thermal and non-thermal dominated emitters, similar to what is observed from non-recycled pulsars.

X-ray emission observed from ms-pulsars which have a spin-down energy of $\dot{E} \geq 10^{35}\,\mathrm{erg\,s^{-1}}$, i.e., PSR J0218+4232, PSR B1821−24 and PSR B1937+21, is caused by non-thermal radiation processes [11, 94, 115]. This is confirmed by their power law spectra (photon-index α in the range 1.5–2, cf. Table 6.7) and pulse profiles which show narrow peaks and have pulsed fractions of up to ∼90–100% (cf. Fig. 6.16). Common in these pulsars is that all show relatively hard X-ray emission, which made it possible to study some of them already with ASCA, BeppoSAX and RXTE. For example, emission from PSR B1821−24 and PSR B1937+21 is

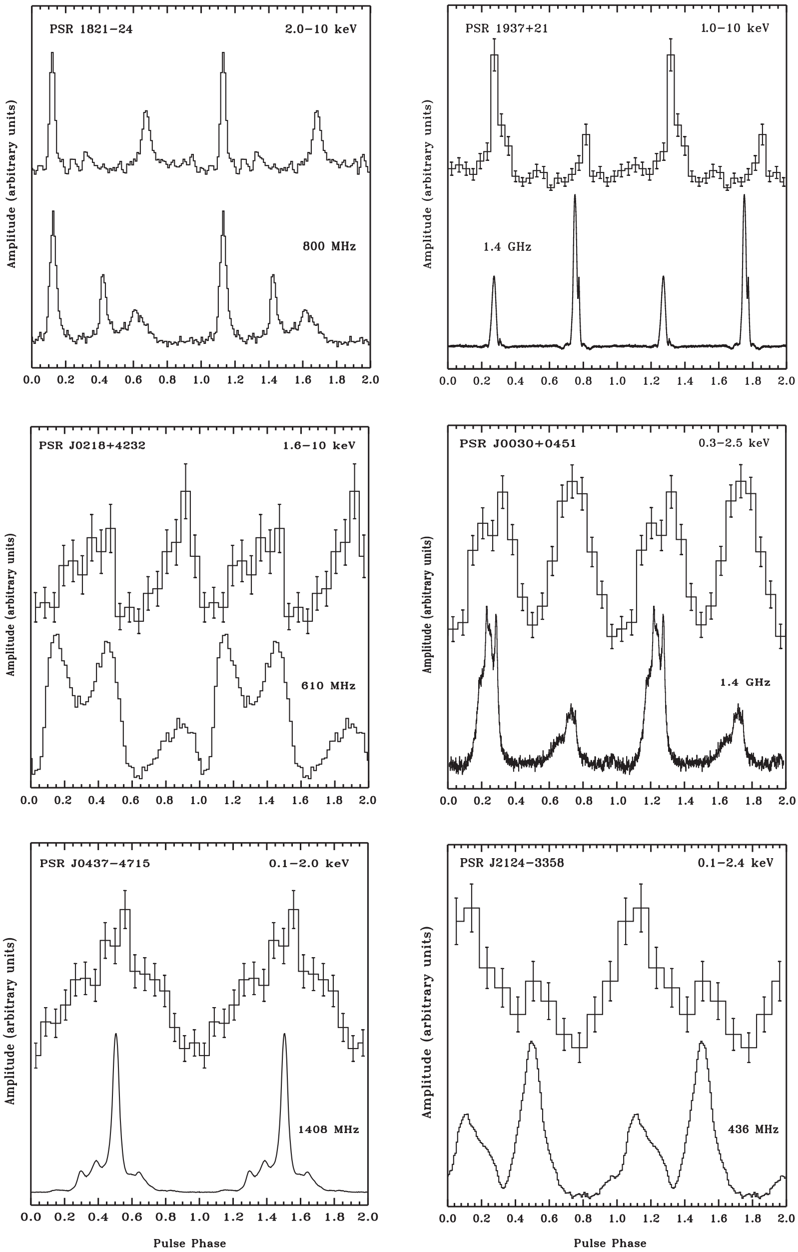

Fig. 6.16 X-ray and radio pulse profiles for the six brightest ms-pulsars. Two full pulse cycles are shown for clarity. The relative phase between the radio and X-ray pulses is only known for PSR 1821−24, B1937+21, 0218+4232 and PSR J0437−4715 with sufficient accuracy. The phase alignment in all other cases is arbitrary

detected by RXTE up to ∼20 keV [110] and PSR J0218+4232 is a candidate for a gamma-ray pulsar [94].

For the remaining ms-pulsars ($P \geq 4$ ms, $\log \dot{E} \sim 33$–34 erg s^{-1}) the X-ray emission is found to be much softer. Their X-ray spectra can be described by compound models consisting of a blackbody plus a power law component (cf. Table 6.7). The latter is required to describe the emission beyond 2–3 keV. For PSR J0437−4715 which is the brightest ms-pulsar detected in X-rays and thus is the one for which the best photon statistics is available, a three component spectral model is required to fit the observed energy spectrum. The model consists of a two temperature blackbody plus a power law model. The X-ray spectrum of PSR J0437−4715 as detected with XMM-Newton is shown in Fig. 6.17.

The relatively small blackbody radii found by these spectral fits suggest that the thermal emission is coming from one or two heated polar-caps whereas the power law component describes the non-thermal radiation emitted from accelerated particles in the co-rotating magnetosphere. The prototypical ms-pulsar of this group, which is still the one for which the best data are available, is the nearest and brightest millisecond pulsar PSR J0437−4715. It was already evident in the ROSAT and ASCA data that its X-ray emission consists of at least two different spectral components [15, 17].

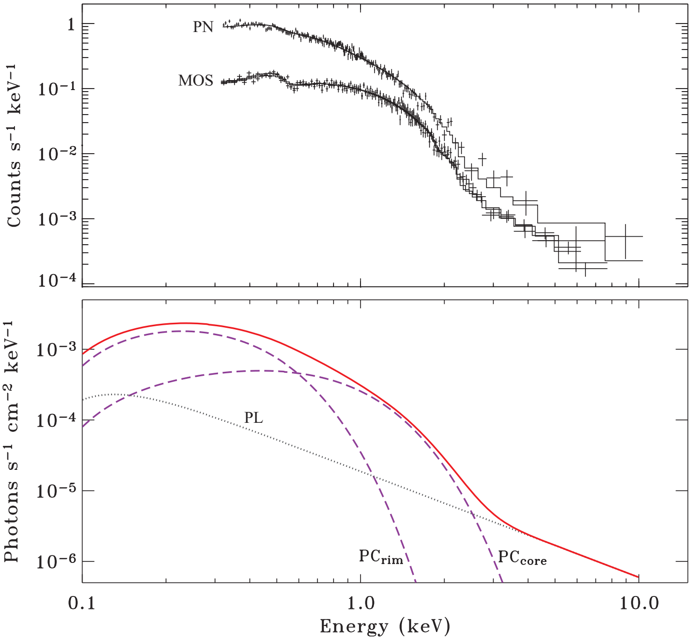

Fig. 6.17 X-ray spectrum of PSR J0437−4715. The *solid curves* show the best fitting model which is the sum of a power law (PL) and a two temperature blackbody model labeled as *core* and *rim*. (From [166])

Chandra and XMM-Newton data have further constrained its emission properties (see [24,166] and Chap. 8). The two thermal components are interpreted as emission from a hot polar cap, having a non-uniform temperature distribution with a hot core ($T_{core} = 1.4 \times 10^6$ K, $R_{core} = 0.4$ km) and a cooler rim ($T_{rim} = 0.5 \times 10^6$ K, $R_{rim} \sim 2.6$ km). The power law component yields a photon index of $\alpha \sim 2.0$. The size of the polar cap is found to be roughly in agreement with the theoretical predictions. Defined as the area of open field lines in which the bombardment by relativistic particles is expected, it is $R_{pc} = R(R\Omega/c)^{1/2}$. Assuming $R = 10$ km for the neutron star radius and taking $\Omega = 1.09 \times 10^3$ for the pulsars angular frequency yields $R_{pc} = 1.9$ km for a polar cap radius of PSR J0437−4715.

Interaction between the relativistic pulsar wind (which carries away the pulsar's rotational energy) and the surrounding interstellar medium is expected to create detectable diffuse emission. If the physical conditions are appropriate this emission takes the form of a pulsar bow-shock nebula as shown in Fig. 6.18.

By now, such diffuse emission is seen in H_α from the black widow pulsar PSR B1957+20 [75,146], from PSR J0437−4715 [19], and from PSR J2124−3358 [50]. Diffuse X-ray emission associated with these bow-shock nebulae could only be detected from PSR B1957+20 [19, 146] and from the solitary ms-pulsar PSR J2124−3358 [82]. For the latter the emission extends from the pulsar to the northwest by ~0.5 arcmin (cf. Fig. 6.18b). Adopting the pulsar distance of ~250 pc, the tail has a length of $\sim 1.1 \times 10^{17}$ cm. The spectrum of the diffuse tail emission can be modeled with a power-law of photon index 2.2 ± 0.3, in line with the emission originating from accelerated particles in the post shock flow. Comparable deep observations to those of PSR J2124−3358 and PSR B1957+20 have been performed by XMM-Newton in previous years on almost all X-ray bright ms-pulsars. For PSR J0437−4715, PSR J0030+0451 and PSR J1024−0719, which

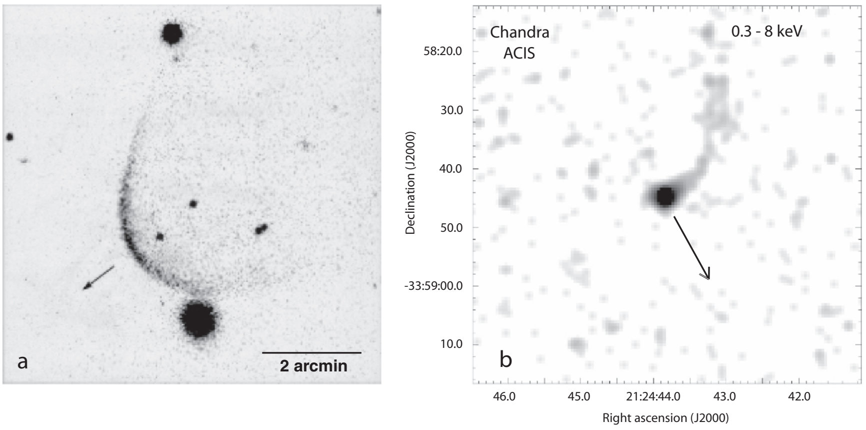

Fig. 6.18 **a** The bow-shock around PSR J0437−4715 as visible in H_α. **b** Chandra image of PSR J2124−3358 and its diffuse, arc-like X-ray emission associated with the pulsar's bow-shock [82]. The pulsars' proper motion directions are indicated

all have spin parameters similar to that of PSR J2124−3358, no diffuse emission was detected down to a $3-\sigma$ limiting flux of $\sim$4–7 $\times\, 10^{-15}$ erg s^{-1} cm^{-2} [82]. The latter suggests that the formation of bow-shocks depends not on the pulsars spin-parameters but might be a function of, e.g., the ISM density and pulsar proper motion.

The majority of the detected ms-pulsars reside in globular clusters. The first millisecond pulsar discovered in a globular cluster was PSR B1821−24A [100] which is located in M28 (NGC 6626). Its inferred pulsar parameters make it the youngest ($P/2\dot{P} = 3.0 \times 10^7$ yrs) and most powerful ($\dot{E} = 2.24 \times 10^{36} I_{45}$ erg s^{-1}) pulsar among all known MSPs (cf. Fig. 6.19 and Table 6.9). Since the *Einstein* era it has been clear that globular clusters contain various populations of X-ray sources of very different luminosities [70]. The stronger sources ($L_x \approx 10^{36}$–10^{38} erg s^{-1}) were seen to exhibit X-ray bursts which led to their identification as low-mass X-ray

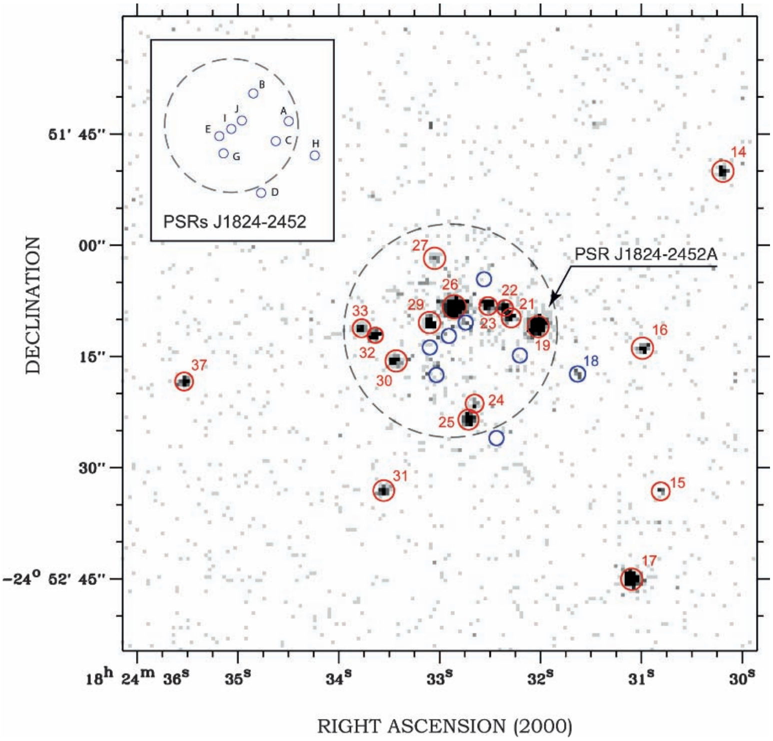

Fig. 6.19 Chandra ACIS image of the central region of the globular cluster M 28. The position of the recently discovered new ms-pulsars are indicated by *blue circles*. Most sources are located within or near to the core-radius (*dashed-circle*). The binary millisecond pulsar PSR J1824−2425H is in agreement with X-ray source #18 [6, 11]. There is faint (only partly resolved) emission near to the center of the cluster. This emission is in agreement with the location of the recently discovered radio pulsars J1824−2425J, J1824−2425I, and J1824−2425E. The *upper left inset* helps to locate the different MSPs. Image from [6]

binaries (LMXBs). The nature of the weaker sources with $L_x \leq 3\times10^{34}$ erg s^{-1} however, was more open to discussion [37,83]. Although many weak X-ray sources were detected in globulars by ROSAT [83, 155], their identification has been difficult due to low photon statistics and strong source confusion in the crowded globular cluster fields, except for a few cases. Of particular interest are the results obtained from Chandra observations of PSR B1821−24A in M28 [11] and on 47 Tuc=NGC 104. From the latter Grindlay [63] reported the detection of 108 sources within a region corresponding to about five times the 47 Tuc core radius. Nineteen of the soft/faint sources (cf. Table 6.9) were found to be coincident with radio-detected millisecond pulsars (MSPs), and Grindlay [62, 63] concluded that more than 50% of all the unidentified sources in 47 Tuc are MSPs. This conclusion is in line with theoretical estimates on the formation scenarios of short-period (binary) pulsars in globular clusters [135]. The application of the Chandra X-Ray Observatory sub-arcsecond angular resolution along with the temporal resolution provided by its HRC-S detector allowed to search for X-ray pulsations from the 47 Tuc millisecond pulsars. This, however, is not just a matter of exposure time. So far, a 830 ksec deep observation found X-ray pulses at a $\sim 4\,\sigma$ level from only three 47 Tuc millisecond pulsars [26].

M28 is the globular cluster with the third largest population of known pulsars. Only in Terzan 5 and 47 Tuc more millisecond pulsars have been found by now. Nine new millisecond pulsars were discovered in M28 in a recent radio survey [18]. Inspecting the archival Chandra data to search for possible X-ray emission from these recently discovered radio pulsars allowed to identify the counterpart CXC 182431−245217 of PSR J1824−2425H, while some faint unresolved X-ray emission near to the center of M28 is found to be coincident with the millisecond pulsars PSR J1824−2452G, J1824−2452J, J1824−2452I and J1824−2452E (cf. Fig. 6.19 and [6]). This finding strongly suggests that indeed a large fraction of the unresolved X-ray emission in globular clusters could be from fainter, so far undiscovered millisecond pulsars [11].

6.4 Summary

By mid 2008, emission from 89 rotation-powered pulsars has been detected in the X-ray band. 47 of these sources belong to the group of field pulsars whereas the other 42 sources are recycled millisecond pulsars. Of the latter, 28 reside in globular clusters (cf. Tables 6.8 and 6.9). Spectral information is available from 78 pulsars (cf. Tables 6.6 and 6.7), but the complexity of the tested models and the accuracy of the fitted spectral parameters are strongly inhomogeneous among the detected sources. This is because different pulsars are detected with different photon statistics, which for fainter sources often allow only to discriminate between basic spectral models such as blackbodies and power laws. This is especially true for the million years old field pulsars and the millisecond pulsars which are generally fainter X-ray emitters. The photon statistics is also the limiting factor in detecting X-ray pulses, although here the fraction of pulsed photons and the duty cycle are important parameters too. By now, X-ray pulses have been detected from 25 field pulsars (e.g., Fig. 6.14) but only from ten millisecond pulsars (e.g., Fig. 6.16 and Table 6.9).

Comparing the emission properties of the 89 detected rotation-powered pulsars gives strong evidence that the observed spectral components and their relative strength vary with the pulsars spin-down age (cf. Fig. 6.20). In young Crab-like pulsars, non-thermal emission dominates. Although these young pulsars should have the highest surface temperature their thermal emission is buried by the even stronger non-thermal magnetospheric emission. However, as the star ages from a few thousand to about hundred thousand years, the non-thermal emission is fading while the star is still hot enough to emit thermal emission from the million degree hot surface. For all middle aged pulsars which are detected with sufficient photon statistics a three component spectral model is required to describe their observed energy spectrum (cf. Fig. 6.20, middle panel). This compound model consist of two thermal components which account for the cooling surface emission and emission from heated polar caps. A third non-thermal component is required to model the emission beyond $\sim$3 keV. In million years old pulsars the star has cooled down to much to show significant cooling emission. Upper limits obtained from the current data, however, are still above the temperatures predicted by thermal evolution models (cf. Fig. 6.13 and Table 6.5). In these million years old pulsars non-thermal radiation takes over again and becomes the dominating emission component (cf. Fig. 6.20, right panel).

Given that the pulsars' emission properties are observed to vary with the spin-down age we checked whether the spectral parameters and/or the pulsars' X-ray efficiency show a spin-down parameter dependence as well. Besides the correction for the interstellar absorption the two parameters which are fitted in power law spectra are the photon-index and the amplitude (usually taken at 1 keV). In Fig. 6.21 the pulse-phase averaged photon-indices of those 54 pulsars which have a non-thermal emission component in their observed X-ray spectrum are plotted as a function of the pulsars' spin-down age. As can be seen from the size of the 1σ error bars the

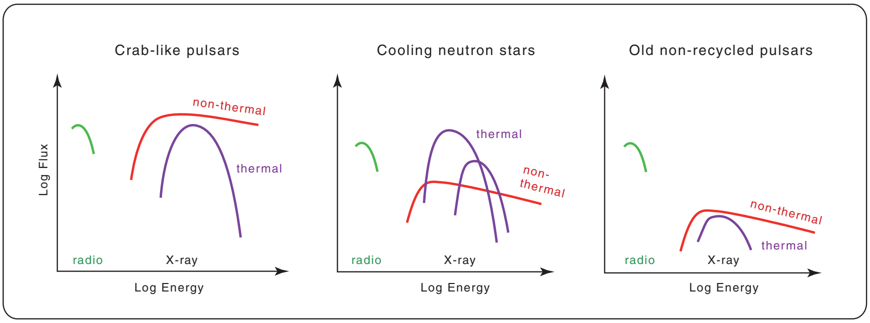

Fig. 6.20 Observed spectral components and their relative strength in rotation-powered pulsars as a function of spin-down age. Non-thermal (*red*) and thermal (*magenta*) spectral components are indicated

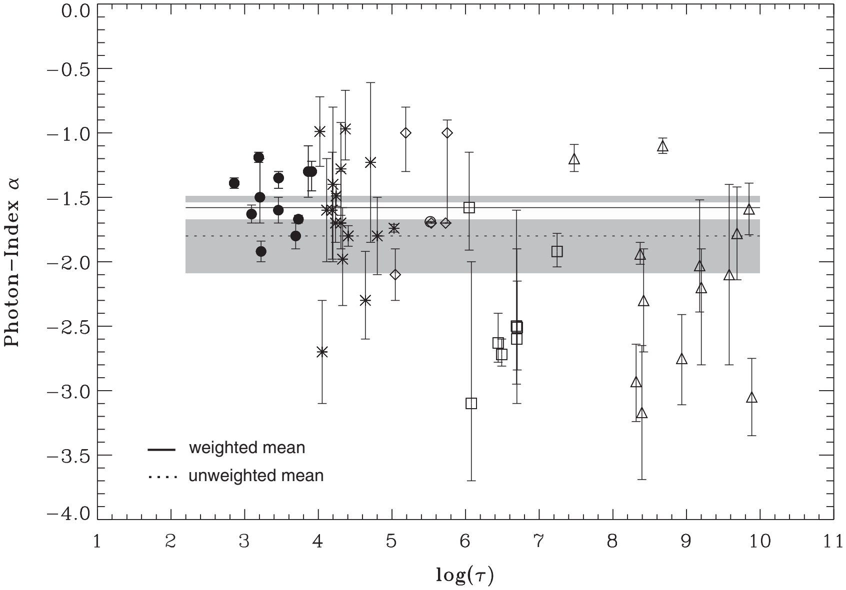

Fig. 6.21 Observed photon-indices as a function of the pulsars' spin-down age. The *solid line* corresponds to the weighted mean, the *dashed line* to the unweighted mean. The *gray shaded/white range* represents the 1σ uncertainty of the unweighted/weighted mean. Symbols are as labeled in Fig. 6.22

data quality varies significantly among those pulsars. Whereas photon-indices from the bright and powerful young pulsars are all measured with relatively high accuracy the uncertainty for most of the older and millisecond pulsars is rather large. Computing the weighted mean (by taking the weight to be the inverse of the size of the error bar) results in an average photon-index of $\alpha = -1.6 \pm 0.07$. This weighted mean, though, is biased by the higher accuracy of the photon-index in younger pulsars, in consequence of a better photon statistics in most of their observed spectra. The unweighted mean yields $\alpha = -1.8 \pm 0.3$. A linear function fitted to all photon-indices doesn't result in an acceptable correlation, in agreement with the large variation of the data points. This is still true, if field and millisecond pulsars are fitted separately. The latter means that the data are still in agreement with having no significant aging effect in the slope of the pulsars' non-thermal X-ray spectra. This result is in agreement with the observation that, e.g., the young Crab-like pulsar B0540−69 and the seventeen million years old pulsar B0950+08 both turn out to have an observed pulse-phase averaged photon-index of $\alpha = -1.92$, even with comparable errors (cf. Table 6.6). It is therefore not justified to conclude that older pulsars in general have softer X-ray spectra.

Chandra and XMM-Newton have obtained spectral information from 78 rotation-powered pulsars. In more than fifty pulsars a power law spectral component is required in the spectral fits. Back in 1997 at the end of the ROSAT mission the number of detected pulsars was roughly only one third of that. Nevertheless, the

ROSAT data allowed for the first time to investigate the spectral emission properties of pulsars for a larger sample, covering a wide range of spin-down ages, magnetic field strengths and spin-periods. With this data Becker and Trümper [15] found the pulsars' X-ray efficiency in the 0.1–2.4 keV band to follow in good approximation the linear trend $L_x = 10^{-3}\,\dot{E}$.

Today, the sample of X-ray detected pulsars is much larger than it was in 1997, including high signal-to-noise spectra from cooling neutron stars, million years old pulsars and recycled millisecond pulsars. The question is whether a linear correlation of the X-ray luminosity as a function of the pulsars' spin-down energy is still in agreement with the new and more significant data. To test this the full sample of X-ray detected pulsars for which spectra have been measured (cf. Tables 6.8 and 6.9) was used to correlate the isotropic X-ray luminosity with the spin-down energy. No beaming correction is applied. As both, emission from heated polar caps and non-thermal emission finally appears to be powered by the rotation of the star the X-ray luminosities from both spectral components were added and correlated with $\dot{E}$. Proper motion corrected period derivatives and spin-down energies were used if available. For the 47 Tuc millisecond pulsars the period derivatives corrected for the influence of the cluster potential were used [24]. Figure 6.22 shows the data points (cf. column L_x^{BB+PL} in Tables 6.8 and 6.9 for the 0.1–2 keV band) with their error bars along with the linear correlation:

$$L_x(0.1\text{–}2\,\text{keV}) = 10^{-3.24^{+0.26}_{-0.66}}\,\dot{E}^{0.997^{+0.008}_{-0.001}}\,. \tag{6.1}$$

The errors in L_x have been fully taken into account and were used to weight the data points. The 1σ-confidence region of the correlation is indicated by the gray shaded bar in Fig. 6.22. The correlation coefficient is found to be $r = 0.9$. As can be seen from the plot the $L_x - \dot{E}$ correlation is still in good agreement with $L_x = 10^{-3}\,\dot{E}$, although it becomes apparent that this relation represents more an upper bound to the X-ray efficiency than a fixed correlation. This was already suggested by Becker and Trümper [15] and is due to the fact that ROSAT by its limited sensitivity detected only the brightest pulsars. With the higher sensitivity of XMM-Newton and Chandra more faint pulsars have been detected for which, e.g., the orientation of the magnetic/rotational axes to the observers line of sight might not be optimal. As no beaming correction can be applied the X-ray efficiency of those pulsars appears to be smaller.

As far as the X-ray efficiency from the 47 Tuc millisecond pulsars are concerned it can be seen from Fig. 6.22 that the X-ray luminosity of these pulsars is well within the scatter of other data points at this spin-down energy level. Within the uncertainties of the deduced X-ray luminosities it is therefore not justified to conclude that these pulsars have an X-ray efficiency which is different from the efficiency observed for field millisecond pulsars.

The X-ray efficiency in the harder X-ray band was investigated by various authors. Seward and Wang [142] used data from the Einstein observatory and found $L_x \propto \dot{E}^{1.39}$ for the 0.2–4 keV energy range. Saito [139] investigated the X-ray efficiency in the 2–10 keV ASCA band by correlating the X-ray luminosities of

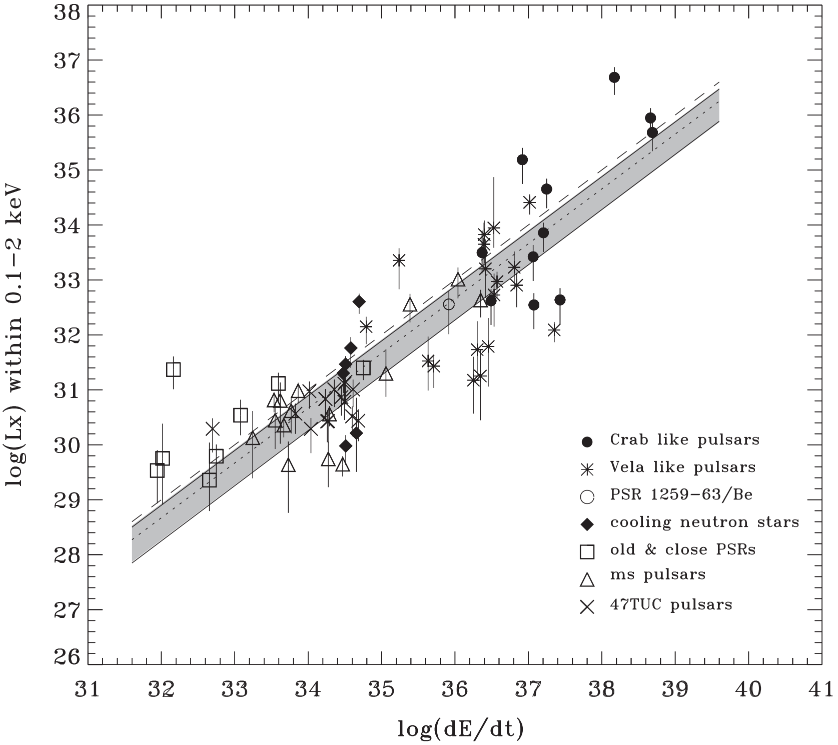

Fig. 6.22 X-ray luminosity of rotation-powered pulsars as a function of the pulsars' spin-down energy. The *dashed line* represents $L_x = 10^{-3}\,\dot{E}$. The *dotted line and gray shaded bar* represent the linear correlation $L_x(0.1\text{–}2\,\text{keV}) = 10^{-3.24}\,\dot{E}^{0.997}$ and its $1-\sigma$ uncertainty range

16 pulsars. They found a relation $L_x \propto \dot{E}^{1.5}$. Possenti et al. [134] found for the 2–10 keV band a correlation $L_x \propto \dot{E}^{1.34}$, although in their work many X-ray luminosities were simply extrapolated from the ROSAT energy range by assuming that the spectrum in the hard X-ray band would be the same as in the soft band. Li et al. [98] investigated the X-ray efficiency by correlating the luminosities of a sample of 27 mostly young pulsars. They found $L_x \propto \dot{E}^{0.92}$ for the energy band 2–10 keV. Figure 6.23 shows the data points L_x^{BB+PL} from Tables 6.8 and 6.9 for the 2–10 keV band along with the fitted linear correlation:

$$L_x(2\text{–}10\,\text{keV}) = 10^{-15.72^{+0.7}_{-1.7}}\,\dot{E}^{1.336^{+0.036}_{-0.014}}\ . \tag{6.2}$$

As for the soft band the errors in L_x were fully taken into account and were used to weight the data points in the linear fit. By reason of a smaller contribution from the thermal spectral components above ∼2 keV the scatter in the data points below $\sim 10^{35}\,\text{erg}\,\text{s}^{-1}$ seems larger. The result from a linear fit, however, is found to be fully in agreement with the earlier results based on Einstein, ASCA and ROSAT data [134, 139, 142].

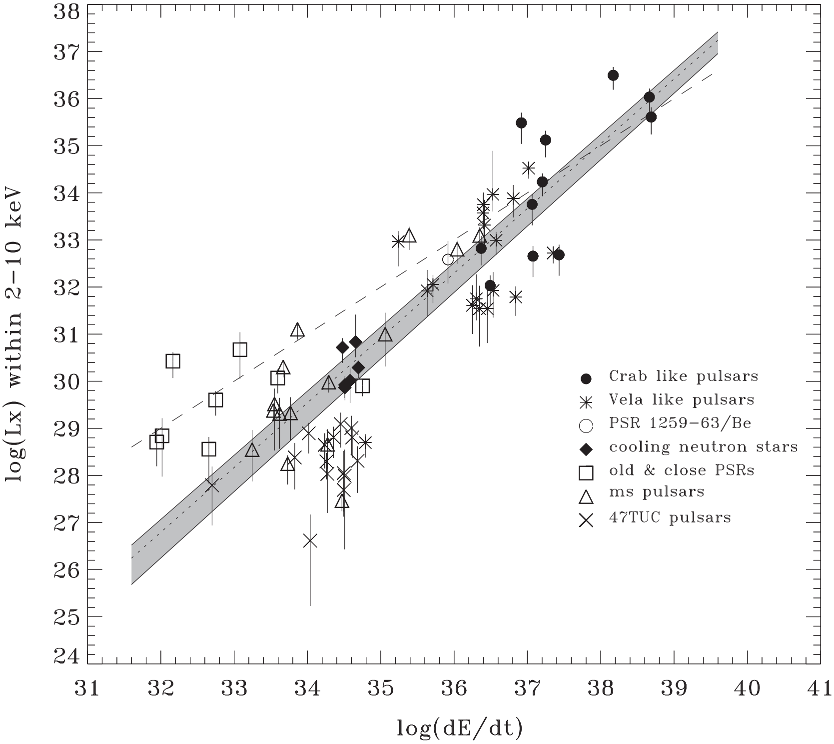

Fig. 6.23 X-ray luminosity (2–10 keV) of rotation-powered pulsars as a function of the pulsars' spin-down energy. The *dashed line* represents $L_x = 10^{-3}\,\dot{E}$. The *dotted line and gray shaded bar* represent the linear correlation $L_x(2\text{–}10\,\text{keV}) = 10^{-15.72}\,\dot{E}^{1.336}$ and its $1-\sigma$ uncertainty range

Albeit the higher sensitivity of Chandra and XMM-Newton which observed the detected pulsars with much better photon statistics than possible in earlier experiments we find the X-ray efficiencies of the rotation-powered pulsars in the soft and hard X-ray bands still in agreement with the earlier measurements [15, 134, 139, 142]. However, what gets conspicuous in the larger data sample is that with an increase in sensitivity also apparently less efficient X-ray pulsars were detected, leading to a larger scatter in L_x vs. $\dot{E}$ for pulsars of the same category. The smaller efficiency, though, does not necessarily mean that the X-ray to spin-down energy conversion process in these pulsars is less efficient but that, e.g., the orientation of the magnetic/rotational axes to the observers line of sight might not be optimal. With an increasing number of detections any linear fit thus will become less correlated. Beaming factors, however, are generally unknown, so that it might be more adequate to express the empirical relation between L_x and $\dot{E}$ without loss of generality in the form:

$$L_x \lesssim 10^{-3}\,\dot{E}\;. \tag{6.3}$$

Table 6.6 Observed spectral properties of X-ray detected rotation-powered field pulsars. (See next page for the column description).

Pulsar	$N_H/10^{21}$ (cm^{-2})	Spectrum	Photon-Index	$T_{cool}^{\infty}/10^5$ (K)	R_{cool}^{∞} (km)	$T_{pc}^{\infty}/10^6$ (K)	R_{pc}^{∞} (km)	Ref.
$B0531+21$	$3.45^{+0.02}_{-0.02}$	PL	$1.63^{+0.07}_{-0.07}$	-	-	-	-	[15, 161]
$B0833-45$	0.22	BB + PL	$2.70^{+0.40}_{-0.40}$	-	-	1.49 ± 0.04	2.10 ± 0.2	[128]
$J0205+6449$	$3.40^{+0.1}_{-0.1}$	PL	$1.67^{+0.03}_{-0.03}$	-	-	-	-	[144]
$J2229+6114$	$6.30^{+1.3}_{-1.3}$	PL	$0.99^{+0.27}_{-0.27}$	-	-	-	-	[65]
$J0633+1746$	0.11	BB + BB + PL	$1.70^{+0.10}_{-0.10}$	5.00 ± 0.1	8.60 ± 1.0	1.90 ± 0.3	0.04 ± 0.01	[43]
$B1951+32$	3.00	PL	$1.74^{+0.03}_{-0.03}$	-	-	-	-	[97]
$B1509-58$	8.60	PL	$1.19^{+0.04}_{-0.04}$	-	-	-	-	[39, 41]
$B1706-44$	5.50	BB + PL	$1.49^{+0.09}_{-0.08}$	-	-	$2.01^{+0.18}_{-0.20}$	$1.81^{+0.43}_{-0.29}$	[105]
$J1357-6429$	$4.90^{+0.20}_{-0.20}$	BB + PL	$1.30^{+0.20}_{-0.20}$	-	-	1.70 ± 0.2	2.50 ± 0.5	[165]
$J1930+1852$	16.0	PL	$1.35^{+0.06}_{-0.10}$	-	-	-	-	[29]
$J1617-5055$	32.0^{+4}_{-4}	PL	$1.30^{+0.10}_{-0.20}$	-	-	-	-	[12]
$B0656+14$	$0.43^{+0.02}_{-0.02}$	BB + BB + PL	$2.10^{+0.30}_{-0.30}$	6.50 ± 0.1	$20.90^{+2.7}_{-3.8}$	1.25 ± 0.03	1.80 ± 0.15	[43]
$J1747-2958$	$27.0^{+1.0}_{-1.0}$	PL	$1.80^{+0.08}_{-0.08}$	-	-	-	-	[48]
$J1124-5916$	$3.10^{+0.40}_{-0.4}$	PL	$1.60^{+0.10}_{-0.10}$	-	-	-	-	[76]
$B1046-58$	$9.00^{4.00}_{-2.00}$	PL	$1.70^{+0.40}_{-0.20}$	-	-	-	-	[56]
$J1811-1925$	$22.2^{+5.70}_{-7.80}$	PL	$0.97^{+0.39}_{-0.32}$	-	-	-	-	[136]
$J0537-6910$	$9.50^{+0.70}_{-0.70}$	PL	$1.80^{+0.10}_{-0.10}$	-	-	-	-	[109]
$B1259-63^a$	$2.90^{+0.20}_{-0.20}$	PL	$1.69^{+0.04}_{-0.04}$	-	-	-	-	[34]
$B1823-13$	7.00	PL	$1.98^{+0.40}_{-0.36}$	-	-	-	-	[125]
$J1420-6048$	22.0	PL	$1.60^{+0.40}_{-0.40}$	-	-	-	-	[137]
$B1800-21$	13.8	PL	$1.40^{+0.60}_{-0.60}$	-	-	-	-	[86]
$J1809-1917$	7.00	PL	$1.23^{+0.62}_{-0.62}$	-	-	-	-	[87]
$B1757-24$	35.0	PL	$1.60^{+0.60}_{-0.50}$	-	-	-	-	[91]
$J1119-6127$	$18.0^{+1.5}_{-0.6}$	BB + PL	$1.90^{+1.10}_{-0.90}$	-	-	2.46 ± 0.12	2.70 ± 0.7	[140]
$B0540-69$	4.60	PL	$1.92^{+0.11}_{-0.11}$	-	-	-	-	[84]
$B1055-52$	$0.27^{+0.02}_{-0.02}$	BB + BB + PL	$1.70^{+0.10}_{-0.10}$	7.90 ± 0.3	$12.30^{+1.3}_{-1.1}$	1.79 ± 0.06	0.46 ± 0.06	[43]
$J1105-6107$	7.00^{+2}_{-2}	PL	$1.80^{+0.40}_{-0.40}$	-	-	-	-	[60]
$B1853+01$	50.0	PL	$1.28^{+0.36}_{-0.36}$	-	-	-	-	[129]
$B0355+54$	8.80	BB + PL	$1.00^{+0.20}_{-1.00}$	-	-	$2.32^{+1.16}_{-0.81}$	$0.12^{+0.16}_{-0.07}$	[104]
$J1509-5850$	$8.0^{+2.3}_{-2.1}$	PL	$1.00^{+0.20}_{-0.30}$	-	-	-	-	[78]
$J0538+2817$	2.21	BB	-	-	-	$2.12^{+0.04}_{-0.03}$	1.68 ± 0.05	[106]
$J2021+3651$	$7.80^{+1.70}_{-1.40}$	PL	$1.70^{+0.23}_{-0.15}$	-	-	-	-	[71]
$B1929+10$	$1.60^{+0.20}_{-0.18}$	PL	$2.72^{+0.12}_{-0.09}$	-	-	-	-	[8]
$B1610-50$	20.0	PL	2.00	-	-	-	-	[132]
$J1846-0258$	39.6	PL	$1.39^{0.04}_{-0.04}$	-	-	-	-	[68]
$J2043+2740$	0.00^{+20}	PL	$3.10^{+1.10}_{-0.60}$	-	-	-	-	[10]
$B1719-37$	$2.40^{+2.4}_{-1.7}$	BB	-	-	-	$2.70^{+0.70}_{-0.58}$	$0.31^{+0.51}_{-0.16}$	[116]
$B0950+08$	$0.26^{+0.27}_{-0.24}$	PL	$1.92^{+0.14}_{-0.12}$	-	-	-	-	[10]
$B2334+61$	$2.60^{+2.6}_{-0.4}$	BB	-	-	-	1.62 ± 0.17	$1.66^{+0.45}_{-0.30}$	[105]
$J0631+1036$	$2.00^{+2.00}_{-1.00}$	PL	$2.30^{+0.38}_{-0.30}$	-	-	-	-	[150]
$B0823+26$	$0.00^{+0.88}$	PL	$2.50^{+0.90}_{-0.45}$	-	-	-	-	[10]
$B1133+16$	0.15	PL	$2.51^{+0.36}_{-0.33}$	-	-	-	-	[90]
$B2224+65$	0.90	PL	$1.58^{+0.43}_{-0.33}$	-	-	-	-	[79]
$J0108-1431$	0.073	PL	$2.20^{+0.24}_{-0.23}$	-	-	-	-	[124]
$B0943+10$	0.43	PL	$2.60^{+0.70}_{-0.50}$	-	-	-	-	[170]
$B0628-28$	$0.62^{+0.31}_{-0.18}$	PL	$2.63^{+0.23}_{-0.15}$	-	-	-	-	[9]

[a] Observed 0.5^0 past apastron

Table 6.7 Observed spectral properties of X-ray detected rotation-powered millisecond pulsars. The individual columns are as follows: (1) Pulsar name; (2) column density (if no error is listed the value was deduced from the radio dispersion measure); (3) spectral components required to fit the observed spectra, PL: power law, BB: blackbody; (4) Pulse-phase averaged photon index; (5) surface temperature; (6) projected blackbody radius of the thermal surface spectral component; (7) polar cap temperature; (8) projected blackbody radius of the thermal polar cap spectral component; (9) references. Errors represent the 1σ confidence interval. If no errors are listed the value represents a best guess.

Pulsar	$N_h/10^{21}$ (cm^{-2})	Spectrum	α	$T^{\infty}_{pc-rim}/10^6$ (K)	R^{∞}_{pc-rim} (km)	$T^{\infty}_{pc-core}/10^6$ (K)	$R^{\infty}_{pc-core}$ (km)	Ref.
J0437 − 4715	0.02	BB+BB+PL	$2.00^{+0.40}_{-0.40}$	0.52 ± 0.16	2.6 ± 0.4	1.40 ± 0.2	$0.12^{+0.04}_{-0.02}$	[14, 17, 167]
J0034 − 0534	0.43	BB	-	-	-	~ 2.20	~ 0.05	[167]
J2124 − 3358	$0.30^{+0.2}_{-0.2}$	BB+PL	$2.10^{+0.70}_{-0.70}$	-	-	1.30 ± 0.1	0.32 ± 0.04	[14, 167]
B1937 + 21	$12.7^{+4.0}_{-3.0}$	PL	$1.1^{+0.15}_{-0.2}$	-	-	-	-	
J1744 − 1134	0.2	PL	2.0	-	-	-	-	[14]
B1257 + 12	0.30	PL	$2.75^{+0.34}_{-0.36}$	-	-	-	-	[126]
B1821 − 24	$1.60^{+0.53}_{-0.61}$	PL	$1.20^{+0.11}_{-0.10}$	-	-	-	-	[11]
J1824 − 2452H	1.8	PL	2 .0	-	-	-	-	[6]
B1957 + 20	0.80	PL	$2.03^{+0.51}_{-0.36}$	-	-	-	-	[75]
J0030 + 0451	$0.125^{+0.095}_{-0.095}$	BB+PL	$3.05^{+0.30}_{-0.30}$	-	-	2.45 ± 0.19	0.075 ± 0.019	[12]
J1024 − 0719	$0.20^{+0.2}_{-0.2}$	BB	-	-	-	2.90 ± 0.3	0.03 ± 0.01	[167]
J0737 − 3039A	0.5	PL	$2.93^{+0.29}_{-0.31}$	-	-	-	-	[31, 89]
J1012 + 5307	0.07	PL	1.78 ± 0.36	-	-	-	-	[156]
J0218 + 4232	0.50	PL	1.10 ± 0.06	-	-	-	-	[157]
B1620 − 26	2.36	PL	$2.30^{+0.40}_{-0.40}$	-	-	-	-	[126]
J1740 − 5340	1.00	PL	~ 1.5	-	-	-	-	[62]
J1911 − 6000C	0.20	PL	2.5	-	-	-	-	[40, 133]
J0751 + 1807	0.40	PL	1.59 ± 0.20	-	-	-	-	[14, 156]
B1534 + 12	0.36	PL	3.17 ± 0.52	-	-	-	-	[89]
J0021 − 72F	0.13	BB	-	-	-	2.19 ± 0.09	0.22 ± 0.11	[24]
J0021 − 72E	0.13	BB	-	-	-	1.75 ± 0.09	0.28 ± 0.17	[24]
J0024 − 7204O	0.13	BB+PL	$1.33^{+0.79}_{-0.79}$	-	-	1.76 ± 0.15	0.28 ± 0.18	[24]
J0024 − 7204U	0.13	BB	-	-	-	2.76 ± 0.22	0.08 ± 0.06	[24]
J0024 − 7204T	0.13	BB	-	-	-	1.56 ± 0.16	0.19 ± 0.17	[24]
J0024 − 7204Q	0.13	BB	-	-	-	2.24 ± 0.2	0.11 ± 0.07	[24]
J0024 − 7204W	0.13	BB+PL	$1.36^{+0.24}_{-0.24}$	-	-	1.52 ± 0.28	0.29 ± 0.29	[24]
J0024 − 7204S	0.13	BB	-	-	-	2.19 ± 0.09	0.22 ± 0.11	[24]
J0024 − 7204R	0.13	BB	-	-	-	2.51 ± 0.16	0.15 ± 0.08	[24]
J0024 − 7204Y	0.13	BB	-	-	-	2.24 ± 0.18	0.11 ± 0.07	[24]
B0021 − 72N	0.13	BB	-	-	-	2.07 ± 0.18	0.13 ± 0.09	[24]
B0021 − 72M	0.13	BB	-	-	-	2.22 ± 0.18	0.11 ± 0.07	[24]
B0021 − 72L	0.13	BB	-	-	-	2.27 ± 0.10	0.20 ± 0.10	[24]
B0021 − 72J	0.13	BB+PL	$1.00^{+0.56}_{-0.56}$	-	-	1.73 ± 0.21	0.22 ± 0.17	[24]
B0021 − 72I	0.13	BB	-	-	-	2.21 ± 0.12	0.18 ± 0.10	[24]
B0021 − 72H	0.13	BB	-	-	-	1.93 ± 0.13	0.17 ± 0.11	[24]
B0021 − 72G	0.13	BB	-	-	-	2.21 ± 0.12	0.18 ± 0.10	[24]
B0021 − 72D	0.13	BB	-	-	-	2.20 ± 0.17	0.13 ± 0.06	[24]
B0021 − 72C	0.13	BB	-	-	-	2.02 ± 0.18	0.11 ± 0.08	[24]

Table 6.8 List of rotation-powered field pulsars that have been detected in the radio, optical, X- and/or γ-ray wavebands, ordered according to their spin-down flux density at Earth $\dot{E}/4\pi d^2$. The individual columns are as follows: 1. Pulsar name; 3–8. Energy ranges in which pulsed (p), unpulsed (d) radiation has been detected: R – radio, O – optical, Xs – soft X-rays ($E_\gamma \sim 1\,\mathrm{keV}$), X_h – hard X-rays ($E_\gamma \sim 10\,\mathrm{keV}$), γ_s – soft γ-rays ($E_\gamma \sim 1\,\mathrm{MeV}$) and γ_h – hard γ-rays ($E_\gamma > 100\,\mathrm{MeV}$). Possible detections are indicated by a question mark. $\dot{E}$ is the pulsar spin-down power; L_x^{PL} is the non-thermal luminosity. L_x^{BB+PL} luminosity from heated polar caps plus non-thermal contributions; $L_x^{BB+BB+PL}$ like L_x^{BB+PL} but plus a surface cooling contribution. η is the X-ray efficiency in the 0.1–2 keV and 2–10 keV bands for the PL spectral component. η^{BB+PL} is the X-ray efficiency in the 0.1–2 keV and 2–10 keV bands for the heated polar caps plus non-thermal components. Radio pulsar parameters have been taken from the ATNF catalog.

Pulsar	Comment	Detected						$\dot{E}/(4\pi d^2)$	$\log\dot{E}$	L_x^{PL}	L_x^{BB+PL}	$L_x^{BB+BB+PL}$	L_x^{PL}	$\log\tau$	P	$\dot{P}\cdot 10^{-15}$	D	$\log B_\perp$	η	η	η^{BB+PL}	Ref.
		R	O	X_s	X_h	γ_s	γ_h	erg/s/cm^2		0.1–2 keV	0.1–2 keV	0.1–2 keV	2–10 keV	yrs	s	s/s	kpc	G	0.1–2 kev	2–10 keV	0.1–2 keV	
B0531+21	Crab	p	p	p	p	p	p	$9.6\cdot10^{-7}$	38.66	$35.95^{+0.18}_{-0.31}$	-	-	$36.03^{+0.18}_{-0.31}$	3.09	0.03308	$4.23\cdot10^{-13}$	2.00	12.58	$1.90\cdot10^{-3}$	$2.30\cdot10^{-3}$	-	[15,161]
B0833−45	Vela	p	p	p	p	p	p	$9.2\cdot10^{-7}$	36.84	$32.81^{+0.25}_{-0.44}$	$32.90^{+0.23}_{-0.40}$	-	$31.79^{+0.37}_{-0.67}$	4.05	0.08932	$1.25\cdot10^{-13}$	0.25	12.53	$9.35\cdot10^{-5}$	$8.86\cdot10^{-6}$	$1.15\cdot10^{-4}$	[16,128]
J0205+6449^a	3C58	p	-	p	-	-	-	$3.3\cdot10^{-8}$	37.43	$32.64^{+0.22}_{-0.45}$	-	-	$32.68^{+0.22}_{-0.45}$	3.73	0.06568	$1.94\cdot10^{-13}$	2.60	12.56	$4.73\cdot10^{-6}$	$2.54\cdot10^{-5}$	-	[144]
J2229+6114^a	G106.6+2.9	p	-	p	-	-	d	$2.0\cdot10^{-8}$	37.35	$32.09^{+0.22}_{-0.45}$	-	-	$32.72^{+0.22}_{-0.45}$	4.02	0.05162	$7.83\cdot10^{-14}$	3.00	12.31	$5.45\cdot10^{-6}$	$2.34\cdot10^{-5}$	-	[65]
J0633+1746	Geminga	p	p	p	-	-	p	$1.0\cdot10^{-8}$	34.51	$29.90^{+0.20}_{-0.35}$	$29.92^{+0.19}_{-0.33}$	$31.41^{+0.21}_{-0.38}$	$29.98^{+0.20}_{-0.35}$	5.53	0.23709	$1.10\cdot10^{-14}$	0.16	12.21	$2.46\cdot10^{-5}$	$2.57\cdot10^{-5}$	$2.95\cdot10^{-5}$	[12,43]
B1951+32	CTB 80	p	-	d	-	-	p	$7.8\cdot10^{-9}$	36.57	$32.97^{+0.18}_{-0.31}$	-	-	$32.95^{+0.18}_{-0.31}$	5.03	0.03953	$5.84\cdot10^{-15}$	2.00	11.69	$2.49\cdot10^{-4}$	$2.41\cdot10^{-4}$	-	[16,97]
B1509−58	MSH 15-52	p	-	p	p	p	-	$5.4\cdot10^{-9}$	37.25	$34.64^{+0.19}_{-0.35}$	-	-	$35.12^{+0.20}_{-0.37}$	3.19	0.15065	$1.54\cdot10^{-12}$	5.20	13.19	$2.54\cdot10^{-3}$	$7.45\cdot10^{-3}$	-	[39,41]
B1706−44	G343.1-02.3	p	-	p	-	-	p	$4.5\cdot10^{-9}$	36.53	$32.20^{+0.46}_{-0.59}$	$32.72^{+0.39}_{-0.58}$	-	$31.93^{+0.30}_{-0.45}$	4.24	0.10245	$9.30\cdot10^{-14}$	2.50	12.49	$4.60\cdot10^{-5}$	$2.48\cdot10^{-5}$	-	[16,105]
J1357−6429		p	-	p	-	-	-	$4.1\cdot10^{-9}$	36.49	$31.66^{+0.22}_{-0.45}$	$32.62^{+0.22}_{-0.45}$	-	$32.03^{+0.22}_{-0.45}$	3.86	0.16610	$3.60\cdot10^{-13}$	2.50	12.89	$1.46\cdot10^{-5}$	$3.47\cdot10^{-5}$	$1.23\cdot10^{-4}$	[165]
J1930+1852^a	G54.1+0.3	p	-	p	-	-	-	$3.8\cdot10^{-9}$	37.06	$33.42^{+0.22}_{-0.45}$	-	-	$33.75^{+0.22}_{-0.45}$	3.46	0.13685	$7.51\cdot10^{-13}$	5.00	13.01	$2.03\cdot10^{-4}$	$4.38\cdot10^{-4}$	-	[29]
J1617−5055	near RCW 103	p	-	p	-	-	-	$3.7\cdot10^{-9}$	37.20	$33.85^{+0.19}_{-0.35}$	-	-	$34.23^{+0.18}_{-0.31}$	3.91	0.06935	$1.35\cdot10^{-13}$	6.00	12.49	$4.49\cdot10^{-4}$	$1.07\cdot10^{-3}$	-	[12]
B0656+14		p	p	p	-	-	?	$3.5\cdot10^{-9}$	34.58	$30.38^{+0.35}_{-0.54}$	$31.76^{+0.20}_{-0.36}$	$32.71^{+0.22}_{-0.45}$	$30.01^{+0.26}_{-0.47}$	5.05	0.38489	$5.50\cdot10^{-14}$	0.30	12.67	$6.36\cdot10^{-5}$	$2.70\cdot10^{-5}$	$1.51\cdot10^{-3}$	[12,43]
J1747−2958	Mouse	p	-	d	-	-	-	$3.3\cdot10^{-9}$	36.40	$33.82^{+0.26}_{-0.23}$	-	-	$33.75^{+0.24}_{-0.23}$	4.41	0.09881	$6.14\cdot10^{-14}$	2.49	12.40	$2.66\cdot10^{-3}$	$2.23\cdot10^{-3}$	-	[48]
J1124−5916^a	G292.0+1.8	p	-	p	-	-	-	$2.7\cdot10^{-9}$	37.08	$32.54^{+0.22}_{-0.45}$	-	-	$32.66^{+0.22}_{-0.45}$	3.46	0.13531	$7.47\cdot10^{-13}$	6.00	13.01	$2.94\cdot10^{-5}$	$3.80\cdot10^{-5}$	-	[76]
B1046−58	Vela twin	p	-	d	-	-	d	$2.3\cdot10^{-9}$	36.30	$31.73^{+0.52}_{-0.46}$	-	-	$31.75^{+0.30}_{-0.43}$	4.31	0.12367	$9.63\cdot10^{-14}$	2.70	12.54	$2.68\cdot10^{-5}$	$2.80\cdot10^{-5}$	-	[56]
J1811−1925	G11.2-0.3	-	-	p	p	-	-	$2.1\cdot10^{-9}$	36.81	$33.23^{+0.29}_{-0.40}$	-	-	$33.88^{+0.18}_{-0.31}$	4.37	0.06466	$4.40\cdot10^{-14}$	5.00	12.23	$2.64\cdot10^{-4}$	$1.17\cdot10^{-3}$	-	[136]
J0537−6910	N157B, LMC	p	-	p	-	-	-	$1.8\cdot10^{-9}$	38.69	$35.68^{+0.19}_{-0.34}$	-	-	$35.61^{+0.20}_{-0.37}$	3.69	0.01612	$5.18\cdot10^{-14}$	47.00	11.97	$9.85\cdot10^{-4}$	$8.34\cdot10^{-4}$	-	[109]
B1259−63^b	Be-star bin	p	-	d	d	d	-	$1.7\cdot10^{-9}$	35.92	$32.55^{+0.25}_{-0.54}$	-	-	$32.58^{+0.39}_{-0.51}$	5.52	0.04776	$2.28\cdot10^{-15}$	2.00	11.52	$4.27\cdot10^{-4}$	$4.57\cdot10^{-4}$	-	[34]
B1823−13	Vela-like	p	-	d	-	-	-	$1.4\cdot10^{-9}$	36.45	$31.80^{+0.52}_{-0.73}$	-	-	$31.55^{+0.38}_{-0.62}$	4.33	0.10146	$7.51\cdot10^{-14}$	4.00	12.45	$2.16\cdot10^{-5}$	$1.22\cdot10^{-5}$	-	[125]
J1420−6048		p	-	p	-	-	-	$1.4\cdot10^{-9}$	37.02	$34.41^{+0.22}_{-0.45}$	-	-	$34.52^{+0.22}_{-0.45}$	4.11	0.06818	$8.32\cdot10^{-14}$	7.70	12.38	$2.48\cdot10^{-3}$	$3.20\cdot10^{-3}$	-	[137]
B1800−21	G8.7-0.1	p	-	d	-	-	-	$1.2\cdot10^{-9}$	36.35	$32.35^{+0.49}_{-0.80}$	-	-	$32.64^{+0.26}_{-0.53}$	4.20	0.13361	$1.34\cdot10^{-13}$	3.80	12.63	$8.01\cdot10^{-6}$	$1.56\cdot10^{-5}$	-	[86]

(Continued)

Table 6.8 (continued)

Pulsar	Comment	Detected						$\dot{E}/(4\pi d^2)$	$\log\dot{E}$	L_x^{PL}	L_x^{BB+PL}	$L_x^{BB+BB+PL}$	L_x^{PL}	$\log\tau$	P	$\dot{P}\cdot 10^{-15}$	D	$\log B_\perp$	η	η	η^{BB+PL}	Ref.
		R	O	X_s	X_h	γ_s	γ_h	erg/s/cm^2		0.1–2 keV	0.1–2 keV	0.1–2 keV	2–10 keV	yrs	s	s/s	kpc	G	0.1–2 kev	2–10 keV	0.1–2 keV	
$J1809-1917$		p	-	d	-	-	-	$1.2\cdot 10^{-9}$	36.25	$31.11^{+0.43}_{-0.61}$	-	-	$31.55^{+0.75}_{-1.46}$	4.71	0.08274	$2.55\cdot 10^{-14}$	3.50	12.17	$8.39\cdot 10^{-6}$	$2.28\cdot 10^{-5}$	-	[87]
$B1757-24$	G5.4-1.2, Duck	p	-	d	-	-	-	$8.6\cdot 10^{-10}$	36.41	$33.10^{+0.54}_{-0.53}$	-	-	$33.21^{+0.26}_{-0.53}$	4.19	0.12492	$1.28\cdot 10^{-13}$	5.00	12.61	$4.90\cdot 10^{-4}$	$6.31\cdot 10^{-4}$	-	[91]
$J1119-6127$	G292.2-0.5	p	-	p	-	-	-	$5.4\cdot 10^{-10}$	36.37	$32.15^{+0.40}_{-0.42}$	$33.50^{+0.40}_{-0.38}$	-	$32.36^{+0.25}_{-0.31}$	3.21	0.40774	$4.02\cdot 10^{-12}$	6.00	13.61	$6.46\cdot 10^{-4}$	$2.17\cdot 10^{-4}$	$1.35\cdot 10^{-3}$	[57]
$B0540-69$	N158A, LMC	p	p	p	p	-	-	$5.0\cdot 10^{-10}$	38.17	$36.68^{+0.19}_{-0.32}$	-	-	$36.49^{+0.21}_{-0.37}$	3.22	0.05035	$4.79\cdot 10^{-13}$	49.40	12.70	$3.27\cdot 10^{-2}$	$2.11\cdot 10^{-2}$	-	[84]
$B1055-52$		p	d	p	-	-	p	$4.4\cdot 10^{-10}$	34.48	$30.70^{+0.22}_{-0.35}$	$31.03^{+0.22}_{-0.37}$	$32.58^{+0.23}_{-0.36}$	$30.72^{+0.58}_{-0.33}$	5.73	0.19710	$5.83\cdot 10^{-15}$	0.75	12.04	$1.66\cdot 10^{-4}$	$1.73\cdot 10^{-4}$	$3.55\cdot 10^{-4}$	[12,43]
$J1105-6107$		p	-	d	-	-	-	$4.2\cdot 10^{-10}$	36.39	$33.65^{+0.39}_{-0.50}$	-	-	$33.57^{+0.18}_{-0.31}$	4.80	0.06319	$1.58\cdot 10^{-14}$	7.00	12.00	$1.79\cdot 10^{-3}$	$1.51\cdot 10^{-3}$	-	[60]
$B1853+01$	W44	p	-	d	-	-	-	$3.9\cdot 10^{-10}$	35.63	$31.53^{+0.44}_{-0.54}$	-	-	$31.92^{+0.19}_{-0.34}$	4.31	0.26744	$2.08\cdot 10^{-13}$	3.00	12.88	$7.81\cdot 10^{-5}$	$1.93\cdot 10^{-4}$	-	[129]
$B0355+54$		p	-	d	-	-	-	$3.5\cdot 10^{-10}$	34.66	$30.21^{+0.64}_{-0.71}$	$30.31^{+0.55}_{-0.63}$	-	$30.83^{+0.57}_{-0.33}$	5.75	0.15638	$4.40\cdot 10^{-15}$	1.04	11.92	$3.59\cdot 10^{-5}$	$1.50\cdot 10^{-4}$	-	[104]
$J1301-6305$		p	-	d	-	-	-	$3.3\cdot 10^{-10}$	36.23	32.30	-	-	-	4.04	0.18452	$2.67\cdot 10^{-13}$	6.62	12.85	-	$1.17\cdot 10^{-4}$	-	
$J1509-5850$		p	-	d	-	-	-	$2.9\cdot 10^{-10}$	35.71	$31.43^{+0.20}_{-0.40}$	-	-	$31.55^{+0.35}_{-0.54}$	5.19	0.08892	$9.17\cdot 10^{-15}$	3.81	11.96	$5.23\cdot 10^{-5}$	$1.93\cdot 10^{-4}$	-	[78]
$J0538+2817$	SNR S147	p	-	p	-	-	-	$2.8\cdot 10^{-10}$	34.69	-	$32.60^{+0.22}_{-0.45}$	-	-	5.79	0.14315	$3.67\cdot 10^{-15}$	1.20	11.87	-	-	$8.1\cdot 10^{-3}$	[106]
$J2021+3651$		p	-	p	-	-	?	$2.8\cdot 10^{-10}$	36.53	$34.13^{+0.23}_{-0.56}$	-	-	$33.97^{+0.18}_{-0.33}$	4.24	0.10372	$9.56\cdot 10^{-14}$	10.00	12.50	$4.03\cdot 10^{-3}$	$2.74\cdot 10^{-3}$	-	[71]
$B1929+10$		p	d	p	-	-	-	$2.5\cdot 10^{-10}$	33.59	$31.12^{+0.20}_{-0.33}$	-	-	$30.07^{+0.18}_{-0.33}$	6.49	0.22651	$1.16\cdot 10^{-15}$	0.36	11.71	$3.32\cdot 10^{-3}$	$2.97\cdot 10^{-4}$	-	[8]
$B1610-50$	Kes 32	p	-	d	-	-	-	$2.4\cdot 10^{-10}$	36.20	$33.25^{+0.22}_{-0.45}$	-	-	$32.98^{+0.22}_{-0.45}$	3.87	0.23169	$4.95\cdot 10^{-13}$	7.30	13.03	$1.13\cdot 10^{-3}$	$6.09\cdot 10^{-4}$	-	[132]
$J1846-0258$[a]	Kes 75	p	-	p	d	-	-	$1.9\cdot 10^{-10}$	36.92	$35.19^{+0.22}_{-0.45}$	-	-	$35.49^{+0.22}_{-0.45}$	2.86	0.32359	$7.10\cdot 10^{-12}$	19.00	13.69	$1.86\cdot 10^{-2}$	$3.70\cdot 10^{-2}$	-	[68]
$J2043+2740$[a]		p	-	d	-	-	-	$1.4\cdot 10^{-10}$	34.75	$31.40^{+0.22}_{-0.45}$	-	-	$29.90^{+0.22}_{-0.45}$	6.08	0.09613	$1.27\cdot 10^{-15}$	1.80	11.55	$4.44\cdot 10^{-4}$	$1.42\cdot 10^{-5}$	-	[10]
$B1719-37$		p	-	d	-	-	-	$8.0\cdot 10^{-11}$	34.51	-	$31.47^{+0.22}_{-0.45}$	-	-	5.54	0.23617	$1.09\cdot 10^{-14}$	1.84	12.21	-	-	$9.05\cdot 10^{-4}$	[116]
$B0950+08$		p	d	p	-	-	-	$6.9\cdot 10^{-11}$	32.75	$29.80^{+0.22}_{-0.36}$	-	-	$29.61^{+0.19}_{-0.33}$	7.24	0.25306	$2.30\cdot 10^{-16}$	0.26	11.39	$1.10\cdot 10^{-3}$	$7.12\cdot 10^{-4}$	-	[10]
$B2334+61$		p	-	d	-	-	-	$5.0\cdot 10^{-11}$	34.79	-	$32.15^{+0.18}_{-0.32}$	-	-	4.61	0.49530	$1.92\cdot 10^{-13}$	3.20	12.99	-	-	$2.28\cdot 10^{-3}$	[105]
$J0631+1036$		p	-	p	-	-	-	$3.3\cdot 10^{-11}$	35.24	$33.36^{+0.22}_{-0.53}$	-	-	$32.77^{+0.34}_{-0.49}$	4.64	0.28777	$1.05\cdot 10^{-13}$	6.55	12.74	$1.31\cdot 10^{-2}$	$3.44\cdot 10^{-3}$	-	[150]
$B0823+26$		p	-	d	-	-	-	$3.2\cdot 10^{-11}$	32.66	$29.36^{+0.69}_{-0.56}$	-	-	$28.56^{+0.26}_{-0.73}$	6.69	0.53066	$1.71\cdot 10^{-15}$	0.34	11.98	$5.02\cdot 10^{-4}$	$7.98\cdot 10^{-5}$	-	[10]
$B1133+16$		p	-	d	-	-	-	$5.6\cdot 10^{-12}$	31.94	$29.46^{+0.37}_{-0.60}$	-	-	$28.66^{+0.29}_{-0.51}$	6.70	1.18791	$3.73\cdot 10^{-15}$	0.36	12.33	$3.86\cdot 10^{-3}$	$5.80\cdot 10^{-4}$	-	[90]
$B2224+65$	Guitar	p	-	d	-	-	-	$2.9\cdot 10^{-12}$	33.08	$30.53^{+0.28}_{-0.37}$	-	-	$30.66^{+0.37}_{-0.62}$	6.05	0.68253	$9.66\cdot 10^{-15}$	1.86	12.41	$2.88\cdot 10^{-3}$	$3.89\cdot 10^{-3}$	-	[79]
$J0108-1431$		p	?	d	-	-	-	$2.9\cdot 10^{-12}$	30.75	$28.41^{+0.21}_{-0.21}$	-	-	$27.93^{+0.30}_{-0.30}$	8.22	0.80756	$7.70\cdot 10^{-17}$	0.13	11.40	$4.57\cdot 10^{-3}$	$1.49\cdot 10^{-3}$	-	[124]
$B0943+10$		p	-	d	-	-	-	$2.1\cdot 10^{-12}$	32.02	$29.75^{+0.63}_{-0.84}$	-	-	$28.84^{+0.38}_{-0.87}$	6.70	1.09770	$3.49\cdot 10^{-15}$	0.63	12.30	$5.43\cdot 10^{-3}$	$6.66\cdot 10^{-4}$	-	[170]
$B0628-28$		p	-	p	-	-	-	$5.8\cdot 10^{-13}$	32.16	$31.37^{+0.24}_{-0.36}$	-	-	$30.42^{+0.19}_{-0.36}$	6.44	1.24441	$7.12\cdot 10^{-15}$	1.45	12.48	$1.62\cdot 10^{-1}$	$1.82\cdot 10^{-2}$	-	[10]

[a] No errors are specified in the literature. A 40% flux uncertainty was assumed.

[b] Pulsar observed at 0.5° apastron.

Table 6.9 List of rotation-powered millisecod pulsars that have been detected in the radio, optical, X- and/or γ-ray wavebands, ordered according to their spin-down flux density at Earth $\dot{E}/4\pi d^2$. The individual columns are as follows: 1. Pulsar name; 3–8. Energy ranges in which pulsed (p), unpulsed (d) radiation has been detected: R – radio, O – optical, Xs – soft X-rays ($E_\gamma \sim 1$ keV), X_h – hard X-rays ($E_\gamma \sim 10$ keV), γ_s – soft γ-rays ($E_\gamma \sim 1$ MeV) and γ_h – hard γ-rays ($E_\gamma > 100$ MeV). Possible detections are indicated by a question mark. $\dot{E}$ is the pulsar spin-down power; L_x^{PL} is the non-thermal luminosity. L_x^{BB+PL} luminosity from heated polar caps plus non-thermal contributions; η is the X-ray efficiency in the 0.1–2 keV and 2–10 keV bands for the PL spectral component. η^{BB+PL} is the X-ray efficiency in the 0.1–2 keV and 2–10 keV bands for the heated polar caps plus non-thermal components. Radio pulsar parameters have been taken from the ATNF catalog.

Pulsar	Comment	Detected						$\dot{E}/(4\pi d^2)$	log$\dot{E}$	L_x^{PL}	L_x^{BB+PL}	L_x^{PL}	log τ	P	$\dot{P}\cdot 10^{-15}$	D	log $B_\perp$	η	η	η^{BB+PL}	Ref.
		R	O	X$_s$	X$_h$	γ_s	γ_h	erg/s/cm^2		0.1–2 keV	0.1–2 keV	2–10 keV	yrs	s	s/s	kpc	G	0.1–2 kev	2–10 keV	0.1–2 keV	
J0437 − 4715	bin	p	d	p	-	-	-	$5.077\cdot 10^{-9}$	33.62	$29.94^{+0.28}_{-0.78}$	$30.81^{+0.33}_{-0.78}$	$29.32^{+0.33}_{-0.75}$	9.20	0.00575	$2.00\cdot 10^{-20}$	0.18	8.76	$2.08\cdot 10^{-4}$	$6.98\cdot 10^{-5}$	$1.53\cdot 10^{-4}$	[14, 17, 167]
J0034 − 0534^{a,b}		p	-	d	-	-	-	$8.488\cdot 10^{-10}$	34.47	-	$29.65^{+0.22}_{-0.45}$	-	9.78	0.00187	$4.96\cdot 10^{-21}$	0.54	7.99	-	-	$1.51\cdot 10^{-5}$	[14, 167]
J2124 − 3358	sol	p	-	p	-	-	-	$7.754\cdot 10^{-10}$	33.55	$29.89^{+0.39}_{-0.63}$	$30.45^{+0.31}_{-0.52}$	$29.52^{+0.33}_{-0.99}$	9.58	0.00493	$1.10\cdot 10^{-20}$	0.27	8.51	$2.18\cdot 10^{-4}$	$9.33\cdot 10^{-5}$	$7.86\cdot 10^{-4}$	[15, 82]
B1937 + 21	sol	p	-	p	-	-	-	$7.097\cdot 10^{-10}$	36.04	$33.01^{+0.22}_{-0.35}$	-	$32.80^{+0.18}_{-0.31}$	8.37	0.00155	$1.05\cdot 10^{-19}$	3.60	8.61	$9.37\cdot 10^{-4}$	$5.78\cdot 10^{-4}$	-	[115]
J1744 − 1134	sol	p	-	d	-	-	-	$6.457\cdot 10^{-10}$	33.28	$29.18^{+0.22}_{-0.45}$	-	$28.91^{+0.22}_{-0.45}$	9.86	0.00407	$8.60\cdot 10^{-21}$	0.26	8.29	$7.94\cdot 10^{-5}$	$4.27\cdot 10^{-5}$	-	[14, 15]
B1257 + 12	sol	p	-	d	-	-	-	$6.288\cdot 10^{-10}$	34.27	$29.74^{+0.31}_{-0.52}$	-	$28.66^{+0.32}_{-0.52}$	8.94	0.00621	$1.14\cdot 10^{-19}$	0.50	8.93	$2.94\cdot 10^{-5}$	$2.43\cdot 10^{-6}$	-	[126]
B1821 − 24	sol, M28	p	-	p	-	-	-	$6.192\cdot 10^{-10}$	36.35	$32.63^{+0.19}_{-0.32}$	-	$33.09^{+0.18}_{-0.31}$	7.48	0.00305	$1.62\cdot 10^{-18}$	5.50	9.35	$1.92\cdot 10^{-4}$	$5.56\cdot 10^{-4}$	-	[11]
B1957 + 20	bin	p	-	d	-	-	-	$5.946\cdot 10^{-10}$	35.06	$31.30^{+0.44}_{-0.43}$	-	$31.00^{+0.46}_{-0.69}$	9.18	0.00160	$1.20\cdot 10^{-20}$	1.50	8.22	$1.74\cdot 10^{-4}$	$8.71\cdot 10^{-5}$	-	[15, 75]
J0030 + 0451	sol	p	-	p	-	-	p	$5.421\cdot 10^{-10}$	33.54	$30.71^{+0.22}_{-0.45}$	$30.81^{+0.22}_{-0.45}$	$29.34^{+0.22}_{-0.45}$	9.89	0.00486	$1.00\cdot 10^{-20}$	0.23	8.35	$1.48\cdot 10^{-3}$	$6.97\cdot 10^{-5}$	$1.86\cdot 10^{-3}$	[12]
J1024 − 0719		p	-	d	-	-	-	$2.925\cdot 10^{-10}$	33.73	-	$29.64^{+0.42}_{-0.88}$	-	9.64	0.00516	$1.85\cdot 10^{-20}$	0.39	8.50	-	-	$8.06\cdot 10^{-5}$	[167]
J0737 − 3039A	bin	p	-	p	-	-	-	$1.963\cdot 10^{-10}$	33.77	$30.62^{+0.23}_{-0.41}$	-	$29.33^{+0.34}_{-0.58}$	8.32	0.02269	$1.76\cdot 10^{-18}$	0.50	9.80	$7.08\cdot 10^{-4}$	$3.62\cdot 10^{-5}$	-	[31, 89]
J1012 + 5307^{a}	bin	p	-	d	-	-	-	$1.441\cdot 10^{-10}$	33.67	$30.36^{+0.22}_{-0.45}$	-	$30.30^{+0.22}_{-0.45}$	9.69	0.00525	$1.71\cdot 10^{-20}$	0.52	8.48	$4.89\cdot 10^{-4}$	$4.30\cdot 10^{-4}$	-	[156]
J0218 + 4232	bin	p	-	p	-	-	-	$6.279\cdot 10^{-11}$	35.39	$32.56^{+0.19}_{-0.33}$	-	$33.10^{+0.18}_{-0.31}$	8.68	0.00232	$7.74\cdot 10^{-20}$	5.70	8.63	$1.02\cdot 10^{-4}$	$3.57\cdot 10^{-4}$	-	[157]
B1620 − 26^{a}	triple sys.	p	-	-	-	-	-	$5.448\cdot 10^{-11}$	34.29	$30.55^{+0.22}_{-0.45}$	-	$29.97^{+0.22}_{-0.45}$	8.42	0.01107	$6.71\cdot 10^{-19}$	1.73	9.44	$1.85\cdot 10^{-4}$	$4.10\cdot 10^{-5}$	-	[126]
J0751 + 1807^{a}	bin	p	-	d	-	-	-	$1.526\cdot 10^{-11}$	33.86	$30.98^{+0.22}_{-0.45}$	-	$31.10^{+0.22}_{-0.45}$	9.85	0.00347	$7.79\cdot 10^{-21}$	2.00	8.22	$1.32\cdot 10^{-3}$	$1.74\cdot 10^{-3}$	-	[156]
B1534 + 12	NS-bin	p	-	d	-	-	-	$1.472\cdot 10^{-11}$	33.25	$30.13^{+0.49}_{-0.74}$	-	$28.55^{+0.42}_{-0.67}$	8.39	0.03790	$2.42\cdot 10^{-18}$	1.00	9.99	$7.61\cdot 10^{-4}$	$2.00\cdot 10^{-5}$	-	[89]
J1824 − 2452H	M28	P	-	d	-	-	-	$9.133\cdot 10^{-12}$	34.51	$29.97^{+0.22}_{-0.45}$	-	$29.70^{+0.22}_{-0.45}$	8.95	0.00462	$2.42\cdot 10^{-20}$	5.50	?	-	-	-	[6]
J1953 + 1846A	M71	p	-	d	-	-	-	-	?	$30.81^{+0.22}_{-0.45}$	-	$30.87^{+0.22}_{-0.45}$	?	0.00488	?	4.00	?	-	-	-	[46]
B0021 − 72F	47-Tuc	p	-	d	-	-	-	$1.689\cdot 10^{-11}$	34.61	-	$31.15^{+0.18}_{-0.32}$	$28.81^{+0.23}_{-0.44}$	8.81	0.00262	$6.45\cdot 10^{-20}$	4.5	8.62	$2.49\cdot 10^{-4}$	$1.57\cdot 10^{-6}$	-	[24]
B0021 − 72E	47-Tuc	p	-	d	-	-	-	$1.288\cdot 10^{-11}$	34.49	-	$30.78^{+0.18}_{-0.33}$	$27.69^{+0.30}_{-0.57}$	8.75	0.00353	$9.85\cdot 10^{-20}$	4.5	8.78	$1.94\cdot 10^{-4}$	$1.58\cdot 10^{-7}$	-	[24]
J0024 − 7204O	47-Tuc	p	-	p	-	-	-	$1.288\cdot 10^{-11}$	34.49	$30.23^{+0.22}_{-0.45}$	$31.11^{+0.21}_{-0.34}$	$28.05^{+0.47}_{-0.82}$	9.14	0.00264	$3.04\cdot 10^{-20}$	4.5	8.46	$4.13\cdot 10^{-4}$	$3.59\cdot 10^{-7}$	$4.72\cdot 10^{-4}$	[24]
J0024 − 7204U	47-Tuc	p	-	d	-	-	-	$1.643\cdot 10^{-11}$	34.60	-	$30.52^{+0.18}_{-0.37}$	$29.01^{+0.26}_{-0.58}$	8.86	0.00434	$9.52\cdot 10^{-20}$	4.5	8.81	$8.28\cdot 10^{-5}$	$2.55\cdot 10^{-6}$	-	[24]
J0024 − 7204T	47-Tuc	p	-	d	-	-	-	$4.501\cdot 10^{-12}$	34.04	-	$30.29^{+0.20}_{-0.44}$	$26.61^{+0.56}_{-1.39}$	8.61	0.00758	$2.94\cdot 10^{-19}$	4.5	9.18	$1.79\cdot 10^{-4}$	$3.78\cdot 10^{-8}$	-	[24]
J0024 − 7204Q	47-Tuc	p	-	d	-	-	-	$7.515\cdot 10^{-12}$	34.26	-	$30.43^{+0.18}_{-0.38}$	$28.29^{+0.18}_{-0.38}$	9.27	0.00403	$3.40\cdot 10^{-20}$	4.5	8.57	$1.46\cdot 10^{-4}$	$1.08\cdot 10^{-6}$	-	[24]

(Continued)

Table 6.9 (continued)

Pulsar	Comment	Detected						$\dot{E}/(4\pi d^2)$	$\log\dot{E}$	L_x^{PL}	L_x^{BB+PL}	L_x^{PL}	$\log\tau$	P	$\dot{P}\cdot 10^{-15}$	D	$\log B_\perp$	η	η	η^{BB+PL}	Ref.
		R	O	X_s	X_h	γ_s	γ_h	erg/s/cm^2		0.1–2 keV	0.1–2 keV	2–10 keV	yrs	s	s/s	kpc	G	0.1–2 kev	2–10 keV	0.1–2 keV	
J0024 – 7204W	47-Tuc	p	-	d	-	-	-	-	?	$30.97^{+0.19}_{-0.48}$	$30.83^{+0.22}_{-0.45}$	$31.29^{+0.23}_{-0.55}$	?	0.00235	?	4.5	?	-	-	-	[24]
J0024 – 7204S	47-Tuc	p	-	d	-	-	-	$9.373\cdot10^{-12}$	34.36	-	$31.01^{+0.18}_{-0.32}$	$28.81^{+0.23}_{-0.44}$	9.53	0.00283	$1.32\cdot10^{-20}$	4.5	8.29	$4.49\cdot10^{-4}$	$2.83\cdot10^{-6}$	-	[24]
J0024 – 7204R	47-Tuc	p	-	p	-	-	-	$1.173\cdot10^{-11}$	34.45	-	$30.87^{+0.18}_{-0.34}$	$29.09^{+0.24}_{-0.50}$	8.77	0.00348	$9.45\cdot10^{-20}$	4.5	8.52	$2.60\cdot10^{-4}$	$4.33\cdot10^{-6}$	-	[24]
J0024 – 7204Y	47-Tuc	p	-	d	-	-	-	$1.990\cdot10^{-11}$	34.68	-	$30.44^{+0.18}_{-0.37}$	$28.31^{+0.31}_{-0.68}$	?	?	?	4.5	?	$5.68\cdot10^{-5}$	$4.22\cdot10^{-7}$	?	[24]
B0021 – 72N	47-Tuc	p	-	d	-	-	-	$7.721\cdot10^{-12}$	34.27	-	$30.43^{+0.19}_{-0.40}$	$28.03^{+0.36}_{-0.83}$	9.56	0.00305	$1.34\cdot10^{-20}$	4.5	8.31	$1.44\cdot10^{-4}$	$5.76\cdot10^{-7}$	-	[24]
B0021 – 72M	47-Tuc	p	-	d	-	-	-	-	?	-	$30.43^{+0.86}_{-0.53}$	$28.27^{+0.86}_{-0.53}$	?	0.00367	?	4.5	?	-	-	-	[24]
B0021 – 72L	47-Tuc	p	-	d	-	-	-	$4.294\cdot10^{-12}$	34.02	-	$30.97^{+0.18}_{-0.32}$	$28.89^{+0.22}_{-0.43}$	9.50	0.00434	$2.12\cdot10^{-20}$	4.5	8.49	$9.03\cdot10^{-4}$	$7.52\cdot10^{-6}$	-	[24]
B0021 – 72J	47-Tuc	p	-	d	-	-	-	$1.329\cdot10^{-11}$	34.51	$30.27^{+0.22}_{-0.45}$	$31.15^{+0.20}_{-0.41}$	$27.99^{+0.56}_{-1.56}$	9.64	0.00210	$7.60\cdot10^{-21}$	4.5	8.11	$4.34\cdot10^{-4}$	$3.05\cdot10^{-7}$	$4.94\cdot10^{-4}$	[24]
B0021 – 72I	47-Tuc	p	-	d	-	-	-	$7.102\cdot10^{-12}$	34.24	-	$30.83^{+0.18}_{-0.34}$	$28.65^{+0.25}_{-0.50}$	9.47	0.00348	$1.86\cdot10^{-20}$	4.5	8.41	$3.40\cdot10^{-4}$	$2.59\cdot10^{-6}$	-	[24]
B0021 – 72H	47-Tuc	p	-	d	-	-	-	-	?	-	$30.56^{+1.03}_{-0.59}$	$27.88^{+1.04}_{-0.60}$	?	0.00321	?	4.5	?	-	-	-	[24]
B0021 – 72G	47-Tuc	p	-	d	-	-	-	$7.102\cdot10^{-12}$	34.24	-	$30.83^{+0.18}_{-0.34}$	$28.65^{+0.25}_{-0.50}$	9.34	0.00404	$2.90\cdot10^{-20}$	4.5	8.54	$3.40\cdot10^{-4}$	$2.59\cdot10^{-6}$	-	[24]
B0021 – 72D	47-Tuc	p	-	p	-	-	-	$2.766\cdot10^{-12}$	33.83	-	$30.57^{+0.18}_{-0.37}$	$28.28^{+0.31}_{-0.68}$	9.51	0.00535	$2.63\cdot10^{-20}$	4.5	8.58	$5.49\cdot10^{-4}$	$1.94\cdot10^{-4}$	-	[24]
B0021 – 72C	47-Tuc	p	-	d	-	-	-	$2.065\cdot10^{-13}$	32.70	-	$30.29^{+0.19}_{-0.43}$	$27.79^{+0.40}_{-0.85}$	9.58	0.00575	$2.43\cdot10^{-21}$	4.5	9.20	$3.90\cdot10^{-3}$	$1.24\cdot10^{-5}$	-	[24]
J1740 – 5340	NGC 6397	p	-	d	-	-	-	$9.837\cdot10^{-11}$	35.13	-	~ 30.9	-	8.54	0.00365	$1.68\cdot10^{-19}$	3.4	8.89	$5.88\cdot10^{-5}$	-	-	[62]
J1701 – 3006B	NGC 6266	p	-	d	-	-	-	-	?	~ 32.62	-	~ 32.35	?	0.00359	?	6.6	?	-	-	-	[36]
J1910 – 5959B	NGC 6752	p	-	d	-	-	-	-	?	~ 30.53	-	~ 29.73	?	0.00835	?	4.5	?	-	-	-	[40]
J1911 – 6000C	NGC 6752	p	-	d	-	-	-	$2.51\cdot10^{-13}$	32.78	~ 30.84	-	~ 30.04	10.58	0.00527	$2.16\cdot10^{-21}$	4.5	8.03	$1.15\cdot10^{-2}$	$1.81\cdot10^{-3}$	-	[40]
J1910 – 5959D	NGC 6752	p	-	d	-	-	-	$2.11\cdot10^{-11}$	34.71	~ 31.06	-	~ 30.79	8.17	0.00903	$9.64\cdot10^{-19}$	4.5	9.47	$2.24\cdot10^{-4}$	$1.20\cdot10^{-4}$	-	[40]

[a] No errors are specified in the literature. A 40% flux uncertainty was assumed.

[b] Photon statistics is not sufficient to distinguish between a thermal and non-thermal spectrum.

6.4.1 Concluding Remarks

The results on the X-ray emission properties of pulsars presented in this chapter and elsewhere in the book demonstrate that X-ray astronomy has made great progress in the past several years thanks to telescopes with larger effective areas and greatly improved spatial, temporal and spectral resolutions. But even in view of these great observational capabilities and the intense neutron star research made over a period of more than 40 years there are fundamental questions which still have not be answered. How are the different manifestations of neutron stars related to each other? What are the physical parameters which differentiate AXPs/SGRs/CCOs/XDINs and rotation-powered pulsars? What is the maximal upper bound for the neutron star mass and what is the range of possible neutron star radii? Is there any exotic matter in neutron stars? Do strange stars exist? And what are the physical processes responsible for the pulsars' broad band emission observed from the infrared to the gamma-ray band? These are just a few of the long standing open questions which can be addressed with the next generation of proposed instruments, eROSITA, Simbol-X and IXO are supposed to bring again a major improvement in sensitivity, making these instruments even more suitable for pulsar and neutron star astronomy.

References

1. Alpar, M.A., Cheng, A.F., Ruderman, M.A., Shaham, J., 1982, Nature, 300, 728
2. Aschenbach, B., Brinkmann, W., 1975, A&A, 41, 147
3. Aschenbach, B., 1998, Nature, 396, 141
4. Bhattacharya, D., van den Heuvel, E.P.J., 1991, Phys. Rep., 203, 1
5. Becker, W., Tennant, A., Kanbach, G., et al., 2008, in preparation, submitted to A&A
6. Becker, W., Hui, C.Y., 2007, A&A, astro-ph/07050119
7. Becker, W., Hui, C.Y., Aschenbach, B., Iyudin, A., 2007, A&A, astro-ph/0607081
8. Becker, W., Kramer, M., Jessner, A., et al., 2006, ApJ, 645, 1421
9. Becker, W., Jessner, A., Kramer, M., et al., 2005, ApJ, 633, 367
10. Becker, W., Weisskopf, M.C., Tennant, et al., 2004, ApJ, 615, 908
11. Becker, W., Swartz, D.A., Pavlov, G.G., et al., 2003, ApJ, 594, 798
12. Becker, W., Aschenbach, B., 2002, in *Neutron Stars, Pulsars and Supernova Remnants*, eds. W. Becker, H. Lesch, J. Trümper, MPE-Report 278, p. 64, (astro-ph/0208466)
13. Becker, W., Pavlov, G.G., 2001, in *The century of Space Science*, eds. J. Bleeker, J. Geiss, M. Huber, Kluwer, Dordrecht, p. 721, astro-ph/0208356
14. Becker, W., Trümper, J., 1999, A&A, 341, 803
15. Becker, W., Trümper, J., 1997, A&A, 326, 682
16. Becker, W., Truemper, J., 1996, A&AS, 120C, 69
17. Becker, W., Trümper, J., 1993, Nature, 365, 528
18. Bégin, S., 2006, Thesis, Faculty of Physics, University of British Columbia
19. Bell, J.F., Bailes, M., Manchester, R.N., Weisberg, J.M., Lyne, A.G., 1995, ApJ, 440, L81
20. Bell, J., 1977, Ann. NY Acad. Sci., 302, 685
21. Beskin, V.S., Gurevich, A.V., Istomin, Ya.N., 1993, Physics of the Pulsar Magnetosphere, Cambridge University Press, Cambridge, ISBN 0-521-41746-5
22. Bisnovatyi-Kogan, G.S., Komberg, B.V., 1974, Sov. Astron., 18, 217

23. Blaschke, D., Glendenning, N.K., Sedrakian, A., 2001, Physics of Neutron Star Interiors, Springer, Berlin, ISBN 3540423400
24. Bogdanov, S., Grindlay, J.E., Heinke, C.O., et al., 2006, ApJ, 646, 1104
25. Bowyer, C.S., Byram, E.T., Chubb, T.A., Friedman, H., 1964, Nature, 201, 1307
26. Cameron, P.B., Rutledge, R.E., Camilo, F., et al., 2007, ApJ, 660, 587
27. Camilo, F., Ransom, S.C., Halpern, J.P., et al., 2006, Nature, 442, 892
28. Camilo, F., Rasio, A.F., 2005, in *Binary Radio Pulsars*, eds. F.A. Rasio, I.H. Stairs, ASP Conf. Ser., 328, p. 147
29. Camilo, F. et al., 2002, ApJ, 574, L71
30. Cassam-Chenai, G., Decourchelle, A., Ballet, J., et al., 2004, A&A, 427, 199
31. Chatterjee, S. et al., 2007, ApJ, 670, 1301
32. Cheng, K.S., Ho, C., Ruderman, M.A., 1986, ApJ, 300, 500
33. Cheng, K.S., Ho, C. Ruderman, M.A., 1986, ApJ, 300, 522
34. Chernyakova, M., et al., 2006, Mon. Not. R. Astron. Soc., 367,1201
35. Chiu, H.Y., Salpeter, E.E., 1964, Phys. Rev. Letters, 12,413
36. Cocozza, G., Ferraro, F.R., POssenti, A., et al., 2008, ApJ 679, L105
37. Cool, A.M., Grindlay, J.E., Krockenberger, M., et al., 1993, ApJ, 410, L103
38. Cordes, J.M., Lazio, T.J.W., 2002, astro-ph/0207156
39. Cusumano, G. et al., 2001, A&A, 375, 397
40. D'Amico, N., Possenti, A., Fici, L., et al., 2002, ApJ, 570, L89
41. DeLaney, T., Gaensler, B.M., 2006, ApJ, 640, 929
42. De Luca, A., Caraveo, P.A., Mereghetti, S., et al., 2006, Science, 313, 814
43. De Luca, A., Caraveo, P.A., Mereghetti, S., et al., 2005, ApJ, 623, 1051
44. De Luca, A., Mereghetti, S., Caraveo, P.A., 2004, A&A, 418, 625
45. Dickel, J.R., Carter, L.M., 1998, MdSAI, 69, 845
46. Elsner, R.F., Heinke, C.O., Lugger, P.M., et al., 2008, submitted to ApJ (astro-ph/08072404)
47. Fesen, R.A., Pavlov, G.G., Sanwal, D., 2006, ApJ, 636, 848
48. Gaensler, B.M. et al., 2004, ApJ, 616, 383
49. Gaensler, B.M., 2004, Adv. Space Res., 33, 645
50. Gaensler, B.M., Jones, D.H., Stappers, B.W., 2002, ApJ, 580, L137
51. Giacconi, R., 1974, in *X-ray Astronomy*, eds R. Giacconi and H. Gursky, R. Reidel, Holland, ISBN 90 277 02950
52. Giacconi, R., Gursky, H., Paolini, F.R., et al., 1962, Phys. Rev. Lett., 9, 439
53. Glendenning, N.K., 2001, Compact Stars, Springer, Berlin, ISBN 0387989773
54. Gold, T., 1968, Nature, 218, 731
55. Gold, T., 1969, Nature, 221, 25
56. Gonzalez, M.E. et al., 2006, ApJ, 652, 569
57. Gonzalez, M.E. et al., 2005, ApJ, 630, 489
58. Gotthelf, E.V., Halpern, J.P., Seward, F.D., 2005, ApJ, 627, 390
59. Gotthelf, V.E., Halpern, J., 2007, ApJ, 664, L35
60. Gotthelf, E.V., Kaspi, V.M., 1998, ApJ, 497, L29
61. Green D.A., 2006, *A Catalogue of Galactic Supernova Remnants (2006 April version)*, Astrophysics Group, Cavendish Laboratory, Cambridge
62. Grindlay, J.E., Camilo, F., Heinke, C.O., et al., 2002, ApJ, 581, 470
63. Grindlay, J.E., Heinke, C.O., Edmonds, P.D., et al., 2001, ApJ, 563, 53
64. Gudmundsson, E.H., Pethick, C.J., Epstein, R.I., 1983, ApJ, 272, 286
65. Halpern, J.P. et al., 2002, *Neutron Stars in Supernova Remnants*, ASP Conference Series, Vol. 271
66. Harding, A.K., Muslimov, A.G., 2001, ApJ, 556, 1001
67. Hwang, U., Kaming, J.M., Badenes, C., et al., 2004, ApJ, 615, L117
68. Helfand, D.J., Collins, B.F., Gotthelf, E.V, 2003, ApJ, 582, 783
69. Helfand, D.J., Becker, R.H., 1984, Nature, 307, 215
70. Hertz, P., Grindlay, J.E, 1983, ApJ, 275, 105
71. Hessels, J.W.T. et al., 2004, ApJ, 612, 389
72. Hester, J.J., Mori, K., Burrows, D., et al., 2002, ApJ, 577, 49

73. Hewish, A., Bell, S.J., Pilkington, J.D.H., et al., 1968, Nature, 217, 709
74. Hoyle, R.A., Narlikar, J., Wheeler, J.A., 1964, Nature, 203, 914
75. Huang, H.H., Becker, W., 2007, A&A, 463, L5
76. Hughes, J.P. et al., 2003, ApJ, 591, L139
77. Hui, C.Y., Becker, W., 2008, A&A, 486, 485
78. Hui, C.Y., Becker, W., 2007, A&A, 470, 965
79. Hui, C.Y., Becker, W., 2007, A&A, 467, 1209
80. Hui, C.Y., Becker, W., 2006, A&A, 454, 543
81. Hui, C.Y., Becker, W., 2006, A&A, 457, L33
82. Hui, C.Y., Becker, W., 2006, A&A., 448, L13
83. Johnston, H.M., Verbunt, F., 1996, A&A, 312, 80
84. Kaaret, P. et al., 2001, ApJ, 546, 1159
85. Kargaltsev, O., Pavlov, G.G., Wong, J.A., 2008, astro-ph/08051041
86. Kargaltsev, O., Pavlov, G.G., Garmire, G.P., 2007, ApJ, 660, 1413
87. Kargaltsev, O., Pavlov, G.G., 2007, ApJ, 670, 655
88. Katsuda, S., Tsunemi, H., Mori, K., 2008, ApJ, 678, L35
89. Kargaltsev, O., Pavlov, G.G., Garmire, G.P., 2006, ApJ, 646, 1139
90. Kargaltsev, O., Pavlov, G.G., Garmire, G.P., 2006, ApJ, 636, 406
91. Kaspi, V.M. et al., 2001, ApJ, 562, L163
92. Kaspi, V.M., Crawford, F., Manchester, R.N., et al., 1998, ApJ, 503, L161
93. Kendziorra, E., Staubert, R., Pietsch, W., et al., 1977, ApJ, 217, L93
94. Kuiper, L., Hermsen, W., Verbunt, F., et al., 2002, ApJ, 577, 917
95. Large, M.I., Voughan, A.E., Mills, B.Y., 1968, Nature, 220, 340
96. Lazendic, J.S., Slane, P.O., Gaensler, B.M., et al., 2003, ApJ, 593, L27
97. Li, X.H., Lu, F.J., Li, T.P., 2005, ApJ, 628, 931
98. Li, X.H., Lu, F.J., Li, Z., 2008, astroph/07074279
99. Lommen, A., Donovan, J., Gwinn, C., et al., 2007, ApJ, 657, 436
100. Lyne, A.G., Brinklow, A., Middleditch, J., et al., 1987, Nature, 328, 399
101. Malofeev, V.M., Malov, O.I., Teplykh, D.A., V.M., 2006, Chin. J. Astron. Astrophys., 6(2), 68
102. Manchester, R.N., Hobbs, G.B., Teoh, A., Hobbs, M., 2005, AJ, 129, 1993
103. Manzali, A., De Luca, A., Caraveo, P.A., 2007, ApJ, 669, 570
104. McGowan, K.E. et al., 2007, Astrophys. Space Sci., 308, 30
105. McGowan, K.E. et al., 2006, ApJ, 639, 377
106. McGowan, K.E. et al., 2003, ApJ, 591, 380
107. Mereghetti, S., Chiarlone, L., Israel, G.L., et al., 2002, in *Neutron Stars, Pulsars and Supernova Remnants*, eds. W. Becker, H. Lesch, J. Trümper, MPE-Report 278, p. 29, astro-ph/0205122
108. Michel, F.C., 1991, Theory of Neutron Star Magnetospheres, University of Chicago Press, Chicago, ISBN 0-226-52331-4
109. Mignani, R.P., et al., 2005, A&A, 431, 659
110. Mineo, T., Cusumano, G., Massaro, E., 2004, A&A, 423, 1045
111. Moffett, D.A., Hankins, T.H., 1996, ApJ, 468, 779
112. Morrison, P., 1958, Nuovo Cimento, 7, 858
113. Morrison, P., Olbert, S., Rossi, B., 1954, Phys. Rev., 94, 440
114. Nasuti, F.P., Mignani, R., Caraveo, P.A., Bignami, G.F., 1997, A&A, 323, 839
115. Nicastro, L., Cusumano, G., Loehmer, O., et al., 2004, A&A, 413, 1065
116. Oosterbroek, T., Kennea, J., Much, R., Cordova, F.A., 2004, Nucl. Phys. B (Proc. Suppl.), 132
117. Ostriker, J.P., Gunn, J.E., 1969, ApJ, 157, 1395
118. Ögelman, H., 2005, in *The Lives of the Neutron Stars*, eds. Alpar, Kiziloglu, van Paradijs, NATO ASI Series, Kluwer, Dordrecht, p. 101
119. Ögelman, H., Finley, J.P., Zimmerman, H.U., 1993, Nature, 361, 136
120. Pacini, F., 1967, Nature, 216, 567
121. Pacini, F., 1968, Nature, 219, 145

122. Page, D., 2007, in Lecture Notes on *Pulsars and Neutron Stars: 40 Years After the Discovery*, eds. W. Becker, Springer, Berlin
123. Page, D., Reddy, S., 2006, ARoNucPS, 56, 1, p. 327
124. Pavlov, G.G., Kargaltsev, O., Wong, J.A., et al., 2008, astro-ph/08030761
125. Pavlov, G.G., Kargaltsev, O., Brisken, W.F., 2008, ApJ, 675, 683
126. Pavlov, G.G. et al., 2007, ApJ, 664, 1072
127. Pavlov, G.G., Teter, M.A., Kargaltsev, O., et al., 2003, ApJ, 591, 1157
128. Pavlov, G.G. et al., 2001, ApJ, 552, L219
129. Petre, R., Kuntz, K.D., Shelton, R.L., 2002, ApJ, 579, 404
130. Petre, R., Canizares, C.R., Kriss, G.A., Winkler, P.F., Jr., 1982, ApJ, 258, 22
131. Pfeffermann, E., Aschenbach, B., 1996, in *Roentgenstrahlung from the Universe*, eds. H.H. Zimmermann, J. Trümper, H. Yorke, MPE Rep. 263, p. 267
132. Pivovareff, M.J., Kaspi, V.M., Gotthelf, E.V., 2000, ApJ, 528, 436
133. Pooley, D., Lewin, W.H.G., Homer, L., et al., 2002, 569, 405
134. Possenti, A. et al., 2002, A&A, 387, 993
135. Rasio, F.A., Pfahl, E.D., Rappaport, S., 2000, ApJ, 532, 47
136. Roberts, M.S.E., et al., 2003, ApJ, 588, 992
137. Roberts, M.S.E., Romani, R.W., Johnston, S., 2001, ApJ, 561, L187
138. Ruderman, M., Sutherland, P.G., 1975, ApJ, 196, 51
139. Saito, Y., 1998, PhD Thesis, University of Tokyo (S98)
140. Safi-Harb, S., Kumar, H.S., 2008, ApJ, 684, 532
141. Seward, F.D., Slane, P.O., Smith, R.K., Sun, M., 2003, ApJ, 584, 414
142. Seward, F.D., Wang Z.R., 1988, ApJ, 332, 199
143. Shibata S., Tomatsuri H., Shimanuki M., et al., 2003, MNRAS, 346, 841
144. Slane, P. et al., 2004, ApJ, 616, 403
145. Staelin, D.H., Reifenstein, III, E.C., 1968, Science, 162, 1481
146. Stappers, B.W., Gaensler, B.M., Kaspi, V.M., et al., 2003, Science, 299, 1372
147. Tananbaum, H., 1999, IAU Circ. #7246
148. Tananbaum, H., Gursky, H., Kellogg, E.M., et al., 1972, ApJ, 174, L143
149. Tennant, A.F., Becker, W., Juda, et al., 2001, ApJ, 554, L173
150. Torii, K., et al., 2001, ApJ, 551, L151
151. Torii, K., Kinugasa, K., Toneri, T., et al., 1998, ApJ, 494, L207
152. Trümper, J.E., Pietsch, W., Reppin, C., et al., 1978, ApJ, 219, L105
153. Tsuruta S., 1998, Phys. Rep., 292, 1
154. Tuohy, I.R., Garmire, G.P., 1980, ApJ, 239, L107
155. Verbunt, F. 2001, A&A, 368, 137
156. Webb, N.A. et al., 2004, A&A, 419, 269
157. Webb, N.A., Olive, J.-F., Barret, D., 2004, A&A 417, 181
158. Weber, F. 1999, Pulsars as Astrophysical Laboratories for Nuclear and Particle Physics, Institute of Physics, ISBN 0-7503-0332-8
159. Weisskopf, M.C., Hester, J.J., Tennant, A.F., et al. 2000, ApJ, 536, L81
160. Wijnand, R., 2005, in *Nova Science Publishers: Pulsars New Research*, astro-ph/0501264
161. Willingale, R., Aschenbach, B., Griffiths, R.G., et al., 2001, A&A, 365, L212
162. Woods, P.M., Thompson, C., 2006, in *Compact Stellar X-Ray Sources*, eds W. Lewin, M. van der Klis, pp. 547–586, Cambridge University Press, Cambridge, ISBN 978-0-521-82659-4, astro-ph/0406133
163. Yakovlev, D.G., Pethick, C.J., 2004, Ann. Rev. Astron. Astrophys. 42, 169
164. Yakovlev, D.G., Levenfish, K.P., Shibanov, Yu.A., 1999, Phys. Usp., 169, 825
165. Zavlin, V.E., 2007, ApJ, 665, L143
166. Zavlin, V.E., 2007, in *Astrophysics and Space Science*, eds. D. Page, R. Turolla, S. Zane, 308, 297
167. Zavlin, V.E., 2006, ApJ, 638, 951
168. Zavlin, V.E., Pavlov, G.G., 2004, ApJ, 616, 452
169. Zavlin, V.E., Pavlov, G.G., Sanwal, D., Trümper, J., ApJ, 540, L25
170. Zhang, B., Sanwal, D., Pavlov, G.G., 2005, ApJ, 624, L109